

Impacts of explicitly simulated gravity waves on large-scale circulation

By

Linda Mudoni

A thesis submitted to the graduate faculty  
in partial fulfillment of the requirements for the degree of

MASTER OF SCIENCE

Major: Meteorology

Program of Study Committee:  
William J. Gutowski Jr., Major Professor  
Tsing-Chang Chen  
Raymond W. Arritt

Iowa State University  
Ames, Iowa  
2005

Copyright © Linda Mudoni, 2005. All rights reserved.

Graduate College  
Iowa State University

This is to certify that the master's thesis of

Linda Mudoni

has met the thesis requirements of Iowa State University

Signatures have been redacted for privacy

## TABLE OF CONTENTS

ABSTRACT	iv
CHAPTER 1. INTRODUCTION	1
1.1 Problem	1
1.2 Background	1
1.3 Research Goals	4
CHAPTER 2. METHODS AND EXPERIMENT DESIGN	6
2.1 Detailed Description of the Model	6
2.2 Methodology	12
2.3 Experiments	12
2.4 Interpolation	14
2.5 Spectral Filtering	15
CHAPTER 3. ANALYSIS OF ZONAL WIND AND EDDY MOMENTUM FLUXES	17
3.1 Zonal Wind and Eddy Momentum Fields	17
3.2 Zonal Wind	17
3.2.1 Change in Resolution	20
3.2.2 Change in Topography	22
3.3 Eddy Meridional Flux of Westerly Momentum	24
3.4 Eddy Vertical Flux of Westerly Momentum	28
CHAPTER 4. ANALYSIS OF GRAVITY WAVES	34
4.1 Introduction	34
4.2 Searching for Gravity Waves	34
4.3 Simulated Wave Properties	41
4.4 Dispersion Relationship	50
4.5 Locally Longitudinally Averaged Eddy Fluxes	57
4.6 Regional (two-dimensional) Simulations at Finer Resolution	60
CHAPTER 5. DISCUSSION AND CONCLUSIONS	65
5.1 Summary	65
5.2 Conclusion	69
5.3 Practical Applications	69
REFERENCES	70
ACKNOWLEDGEMENTS	73

**ABSTRACT**

In past studies gravity wave effects in global circulation models were simulated via envelope orography or gravity wave parameterization. Gravity waves are simulated in a simplified global model by passing stable stratified air over an idealized mountain. A 3-D anelastic model in a dry environment with varying horizontal resolution and uniform vertical resolution was used for gravity-wave simulation and analysis. The model used flat terrain except for an idealized Andes mountain (5000 m high) in the Southern Hemisphere. Higher resolution is attained near the idealized mountain through grid stretching, which gives variable resolution to the whole domain. The main objective of this study is to investigate the generation of gravity waves and their effect on the large-scale flow. Effects of different model configurations on the eddy momentum fluxes and hence the zonal flow were tested. Simulated wave properties were consistent with the gravity wave theory. High-resolution, 2-D regional simulations at different resolutions were compared to the 3-D model output of vertical wind. The finest resolution in the 3-D model resolved gravity waves and the coarser resolutions could not. The wave structure for the finest resolution 3-D simulation compared well with the 2-D regional simulations. Simulated vertical eddy fluxes of momentum by gravity waves produced accelerations of several meters per second per day and were large enough to have significant influence on the zonal flow.

## CHAPTER 1

### INTRODUCTION

#### 1.1 Problem

Much gravity-wave research in the past using global models has focused on using gravity-wave parameterization or implicit effects via envelope orography. Experiments by McFarlane (1987) showed that introducing gravity-wave-drag parameterization in a global climate model (GCM) improved the large-scale flow in the Northern Hemisphere but caused little change in the Southern Hemisphere. The wave drag reduced substantially the wind speeds in the mean zonal wind in the Northern Hemisphere. Introduction of drag also resulted in a big separation between the polar night jet and the midlatitude jet.

In our study we want to simulate gravity waves explicitly in a global model-using grid stretching to give fine resolution to a mountain region. Rabinovitz et al. (2000) introduced an orographic-forcing in a uniform resolution GCM, a variable resolution GCM using nested grids and a stretched-grid GCM that may have had gravity waves in the high-resolution region. However, they were not diagnosed. We will examine explicitly simulated gravity waves and their direct influence, as opposed to parameterized drag, on the evolution of the large-scale circulation.

#### 1.2 Background

In the past three decades much work has been done on gravity waves in global models at low resolution, using gravity-wave drag parameterizations. Improvement in

computational speed has allowed the resolution in GCMs to increase substantially over the years. GCMs now can resolve features at mesoscale level or smaller, though this is not typical.

Gravity waves, also known as buoyancy waves, are oscillations of air parcels produced by the lifting force of positive buoyancy and the restoring force of gravity. Individual parcels of air are displaced alternately upward and downward from their buoyantly neutral equilibrium position as they oscillate.

Vertically propagating waves, where the phase varies with height, are known as internal gravity waves. Internal gravity waves exist in a stably stratified atmosphere (Holton 1982). These waves generally have weak influence on synoptic weather but are important at the mesoscale level. They are known to transport energy and momentum to high levels such as the stratosphere and the mesosphere (Lindzen 1981, Holton 1982, Garcia and Solomon 1985 and McFarlane 1986). The momentum deposited due to gravity-wave breaking can alter the mean zonal state (Garcia and Solomon 1985).

Gravity waves have also been a major source of clear air turbulence (Knox 1997), which is a top hazard to aircraft (de Villiers and van Heerden 2001, Clark et al. 2000 and others). They also trigger instabilities that cause severe weather (Hooke 1996). There are many causes of gravity waves such as flow of stably stratified air over irregular terrain, the onset of shear instability, rapid development of convective complexes, and squall lines (McFarlane 1987). In our study, we simulate gravity waves by passing stably stratified air over a mountain (Lilly 1982).

Numerical experiments done by Holton (1982) have revealed that mechanical dissipation resulting from breaking of vertically propagating gravity waves plays an

important role in the general circulation of the mesosphere. Wave absorption occurs at critical levels when the Richardson number exceeds 25 (McFarlane 1987). The dissipation or absorption of gravity waves of sufficient magnitude and horizontal extent could modify the large-scale mean flow in the atmosphere through wave momentum-flux convergence or divergence (e.g., McFarlane 1987, among others). Observational data has revealed (Lilly 1983) that gravity-wave momentum flux convergence that is associated with orographically excited waves might occur in the upper troposphere and lower stratosphere. Could this convergence affect the general circulation in the stratosphere or troposphere?

Before general circulation models accounted for gravity wave drag, they revealed a westerly bias as resolution increased (Palmer et al. 1986, and McFarlane 1987). Using a GCM, Slingo and Pearson (1986) did two simulations to solve the westerly bias problem: one with envelope orography in the model and one with parameterization of the effects of orographic gravity-wave drag. They compared these to a control run. In both cases there were significant changes in the climatology of the model. Results using the gravity-wave scheme were very close to the observations in both hemispheres for both winter and summer. The summer flow for the simulation with the envelope orography was distorted versus reality. In the envelope orography experiment reduced the westerlies through, excessive increase in the mountain-pressure torque. The gravity-wave drag, instead, decreased the westerly bias without such excessive mountain torque. Slingo and Pearson (1986) postulated that, with sufficiently high horizontal resolution, the major effects of mountains (gravity waves) would be resolved.

McFarlane (1987) also studied the westerly bias problem in the mid-latitudes. Introduction of a gravity-wave drag (GWD) scheme improved the simulated zonal flow

structure. Inclusion of the GWD with the model's standard orography, resulted in a slight decrease in the meridional eddy heat, momentum and other fluxes. Addition of GWD to the envelope orography did not decrease fluxes. Wave-drag parameterizations had less impact on the large-scale flow in the Southern Hemisphere for all seasons compared to the Northern Hemisphere. A question which arises is: How does the gravity-wave momentum convergence or divergence modify the large-scale mean flow in the troposphere?

Kim et al. (1996) used envelope orography and a GWD parameterization developed by Kim and Arawaka (1995) to increase the surface drag in the UCLA GCM, thus adding drag to the free atmosphere, and reducing a westerly bias (Palmer et al. 1986, and McFarlane 1987). The use of a GWD parameterization together with envelope orography resulted in the improvement of the ensemble mean flow for January.

### **1.3 Research Goals**

The explicit simulation of gravity waves in global models with variable resolution appears not to have been examined. We will use a dynamic grid adaptation (DGA) model (Prusa and Smolarkiewicz 2003) in our studies. In this model grid points can move with a changing target or they can focus higher resolution on a fixed region. This type of model allows one to increase the resolution locally at the expense of coarser resolution in the areas away from the focus region. Prusa et al. (1996), among others, have studied the upward propagation and breaking of gravity waves forced at the tropopause. Our study will focus on the troposphere. We are interested in gravity waves generated by stratified air moving over an obstacle, in this case irregular terrain.



We will run a model with idealized topography for a long enough period of time for gravity waves to break and possibly influence the large-scale flow. The simulations will be divided into high and low resolution (defined in Chapter 2). They are tested with and without topography. One question arises: What is the lowest resolution at which gravity waves can be simulated in our model? To address this question a number of simulations will be carried out with a global model in which the resolution is varied. A more detailed description of the simulations and methods used appears in Chapter 2. We will look at the eddy fluxes of momentum and zonal averages of zonal velocity to see how the orography influences the structure of the large-scale flow in our model (Chapter 3). In addition to this, we will also examine the properties of gravity waves using vertical cross sections of vertical velocity fields that are filtered in zonal wave number (Chapter 4). A discussion and conclusion of the findings appears in Chapter 5.

## CHAPTER 2

### METHODS AND EXPERIMENT DESIGN

#### 2.1 Detailed Description of the Model

This study uses a global model with some simulations using relatively high resolution at a localized place on the globe through grid stretching. Prusa and Smolarkiewicz (2003) describe details of the dynamics code. The focus of the study is the Southern Hemisphere. The model has flat terrain except some runs include an idealized Andes mountain range. All the simulations used 41 vertical levels, 750 m apart and the lowest level is at the surface. Low-resolution (LR) runs use a 65x32 lon-lat grid that may be uniform or stretched. High-resolution (HR) runs use a 128x64 lon-lat grid. Table 1 gives a detailed description of the model configuration used. The idealized mountain range has height defined by:

$$zs(rad, a) = ae^{-rad^4} \quad (2.0)$$

where  $zs$  is the height of the mountain,  $a$  is 5000 m, and  $rad$  is the scaled distance from the peak,

$$rad(xx, yy) = \sqrt{(xx/xml)^2 + (yy/yml)^2} \quad (2.1)$$

where  $xx$  is east-west distance (degrees-longitude) from the mountain's central longitude and  $yy$  is the north-south distance (degrees-latitude) from the central latitude. Here,  $xml=2.5^\circ$  and  $yml=25^\circ$ . For these simulations the central latitude is  $20^\circ$  S and the central longitude is  $180^\circ$  (Fig. 1). At a distance of  $rad=1$  the elevation is 1845m.

Table 1 Model configuration used in the study.

Experiment	Horizontal Resolution	Description	Grid distribution	Absorbers	Time step (Mins)
LRUGF	Low resolution (65x32) global lon-lat grid	Flat terrain (F)	Uniform grid (UG) (6.25° x 6.25°) lon-lat	Vertical sponges- 20km and above	15
LRSGF	Low resolution (LR) (65 x 32) global lon-lat grid	Flat terrain (F)	Stretched grid Highest grid resolution is (2.8° x 1.9°) lon-lat	Vertical sponges- 20km and above	7.5
LRUGT	Low resolution (65 x 32) global lon-lat grid	Mountain (T)	Uniform grid (UG) (6.25° x 6.25°) lon-lat	Vertical sponges- 20km and above	7.5
LRSGT	Low resolution (LR) (65 x 32) global lon-lat grid	Mountain (T)	Stretched grid (SG) grid . Resolution near mountain is (2.8° x 1.9°) lon-lat	Vertical sponges- 20km and above	7.5
HRUGT	High resolution (HR) (128 x 64) global lon-lat grid	Mountain (T)	Uniform grid (UG) (2.8° x 2.8°) lon-lat	Vertical sponges- 24km and above	7.5
HRS GT	High resolution (HR) (128 x 64) global lon-lat grid	Mountain (T)	Stretched grid (SG) Resolution near mountain is (1.4°x0.9°) lon-lat	Vertical sponges- 24km and above	6.0

The global model is anelastic, and only dry simulations are computed in this study.

Top and bottom boundaries use slip boundary conditions for horizontal winds and have zero vertical velocity. The model has a sponge layer near the top so that upward propagating gravity waves are not reflected. The damping extends from 20-30 km in the LR runs and from 24-30 km in the HR runs. Damping also occurs at all levels within 15° of the poles. Consequently undamped results occur in the region between 0-20 km, and -65° to +65° latitude.

#### (a) Vertical Sponge layers

The vertical sponge layers provide the damping needed to prevent or minimize top boundary wave reflections. Correct damping will provide sufficient absorption of the wave;

and is a function of the absorber time scale and depth. The bottom of the sponge layer is set at an altitude of  $z = z_{ab} = 20$  km for the lower resolution runs; giving a total absorber depth of 10 km, and  $z_{ab} = 24$  km for the highest resolution runs, giving a total depth of 6 km. Below this altitude, there is no damping. Above this altitude, the absorber strength increases linearly to a minimum damping time of  $\tau_{owz} = 0.1$  days at the top of the domain. This means the absorber causes significant dissipation of waves with wavelength of  $\sim 10$  kms and periods of  $\sim 0.1$  day. The absorber damps a spectrum of waves, though it is tuned to damp 10 km, 0.1 day waves most aggressively.

### (b) Model Forcing

Forcing in the model uses Newtonian relaxation of the potential temperature field to a zonally symmetric equilibrium temperature (Held and Suarez 1994):

$$\frac{\partial \theta}{\partial t} = \dots - k_T(\phi, \sigma) [\theta - \theta_{eq}(\phi, p)] \quad (2.2)$$

$$\sigma = p/p_0 \quad (2.3)$$

where  $k_T$  is the inverse of the radiative relaxation time for temperature forcing,  $\phi$  is latitude,  $p$  is pressure and  $p_0$  is a reference pressure. The radiative relaxation time is given by.

$$k_T = k_a + (k_s - k_a) \max\left(0, \frac{\sigma - \sigma_b}{1 - \sigma_b}\right) \cos^4 \phi \quad (2.4)$$

where parameter values appear in Table 2 . The assumed radiative equilibrium temperature distribution was discussed by Held and Suarez (1994) and is given by

$$\theta_{eq} = \max \{200K, (p/p_0)^K [315 - (\Delta \theta)_y \sin^2 \phi - (\Delta \theta)_z \log (p/p_0) \cos^2 \phi]\}, \quad (2.5)$$

Held and Suarez (1994) used a standard case, followed here, in which the horizontal forcing parameter  $(\Delta\theta)_y$  was 60 K, and the vertical forcing parameter  $(\Delta\theta)_z$  was 10 K.

The largest time scale in the model is 40 days  $(1/k_a)$ . We assume that the spin up time to simulate properly the response to Held Suarez (1994) forcing will be a few times the inverse of  $k_a$ . As we will see later, our low resolution runs with grid stretching and high-resolution runs had a spin up time of 120 days. However the spin up time for low-resolution runs with uniform grid was two times this.

Low-level winds experience a Rayleigh damping that corresponds to boundary-layer friction and is given by (Held and Suarez 1994),

$$\frac{dv}{dt} = \dots - k_v(\sigma)v, \quad (2.6)$$

where  $k_v$  is a linear damping coefficient that varies with  $\sigma$ . Damping is from  $\sigma = 1$  to  $\sigma = 0.7$  (~700mb).

$$k_v = k_f \max\left(0, \frac{\sigma - \sigma_b}{1 - \sigma_b}\right). \quad (2.7)$$

$k_f = 1 \text{ day}^{-1}$ , and  $\sigma_b$  is defined in Table 2. It is assumed that  $k_v \neq 0$  only in layers close to the surface i.e.  $\sigma > 0.7$ .

Table 2. Parameter values used in this study.

$\sigma_b$	$k_f$ (day <sup>-1</sup> )	$k_s$ (day <sup>-1</sup> )	$k_a$ (day <sup>-1</sup> )	$(\Delta\theta)_y$ K	$(\Delta\theta)_z$ K	$p_0$ mb
0.7	1	1/4	1/40	60	10	1000

### (c) Model Equations

The model uses the anelastic approximation, which requires a basic state temperature and density that are functions of height only. This state must be in hydrostatic balance. Our basic state also has no flow. The anelastic model equations for deviations about the basic state are:

$$\nabla \cdot \rho_b \mathbf{V} = 0 \quad (2.8)$$

$$\frac{d\mathbf{V}}{dt} = -\nabla(\pi') - g \frac{\theta'}{\theta_b} + \mathbf{F} \quad (2.9)$$

$$\frac{d\theta'}{dt} = -\mathbf{V} \cdot \nabla \theta_e \quad (2.10)$$

where  $\theta' = \theta - \theta_e$ ,  $\theta_e$  is the environmental reference profile (Prusa and Smolarkiewicz 2003), which describes an undisturbed geostrophically balanced state,  $\mathbf{V}$  is the three dimensional velocity vector and  $\mathbf{F}$  is the inertial force. The symbols  $\theta$ ,  $\rho$  and  $\pi'$  represent potential temperature, density and density normalized pressure and  $g$  is the gravity acceleration. It is

assumed that  $\frac{\rho' - \rho_b}{\rho_b} \ll 1$  and  $\frac{\theta' - \theta_b}{\theta_b} \ll 1$ , where  $\rho_b$  and  $\theta_b$  are the basic state

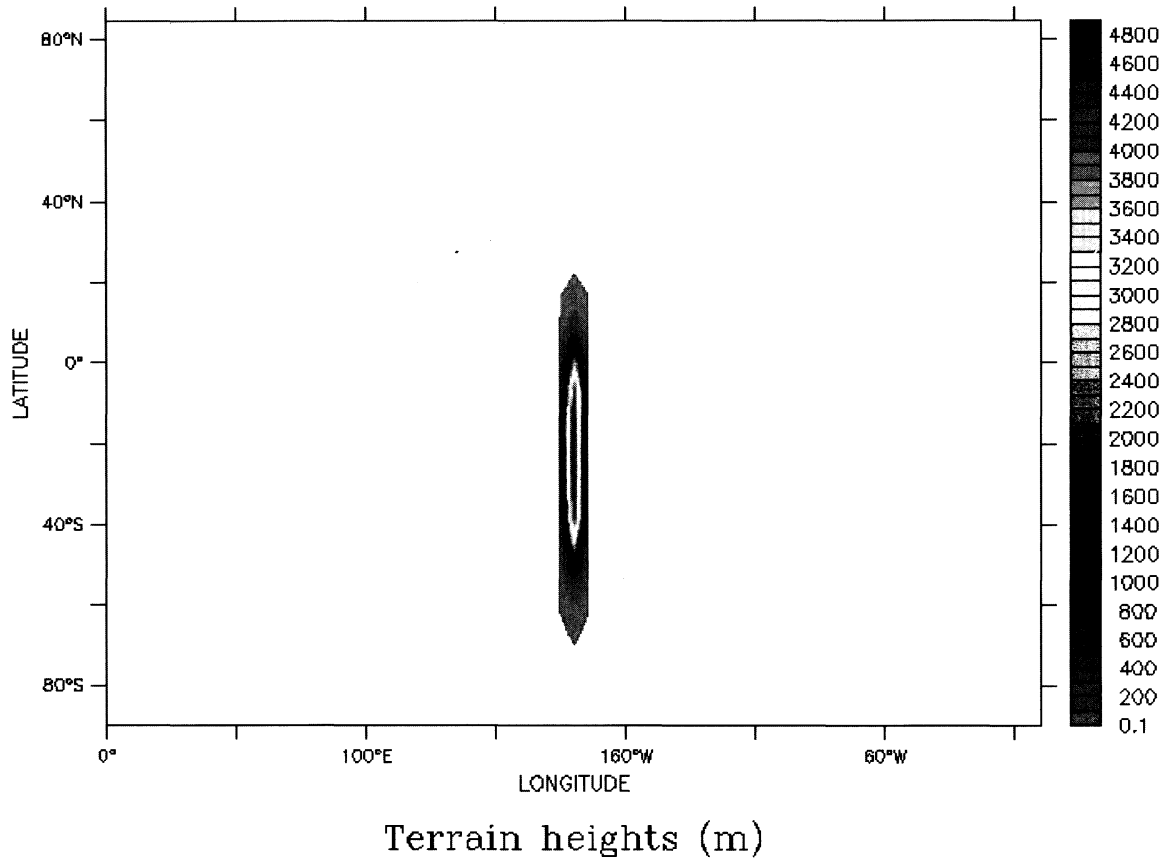


Fig. 1 Terrain heights for the idealized Andes mountain centered at (20° S, 180° E). The highest peak on the mountain is 5000 m . The topography falls exponentially in the east-west and north/south directions.

density and potential temperature, respectively, and the primes represent the deviations about the environmental state. Also required is that  $H_t \gg 1/k$  where  $H_t$  is the scale height for potential temperature , and  $k$  is the vertical wave number of disturbances being computed. That is, the potential temperature scale height must be much larger than the vertical scale of any dynamical structures. This is needed for the anelastic approximation to conserve energy globally (Lipps and Hemler 1982). The model uses a specified solution to the anelastic equations termed the environmental state. It is a steady state and zonally symmetric solution.

The model then computes deviations from this state to obtain the full, three dimensional, time varying solutions that include the non-geostrophic behavior of the model.

## 2.2 Methodology

As noted earlier, various simulations were performed in two classes: high and low resolution. Experiments were performed with and without topography. The vertical coordinate follows the terrain (Gal-Chen and Somerville 1975). A number of variations in the horizontal resolution of the model were made which are explained in more detail later and in Table 1. The model was run on a single processor computer by the author for the low-resolution experiments and on a parallel processing computer by Dr. J. Prusa for the high-resolution experiments. The highest resolution of  $1.4^\circ \times 0.94^\circ$  (or about  $150 \times 100$  km) was obtained using a stretched grid near the mountain.

The model was spun up for 120 days for low-resolution runs with stretched grid and high-resolution runs to reach a quasi-equilibrium state. Uniform grid runs at low resolution were spun up for 240 days. After spin up, integrations to predict the state of the atmosphere continued for up to 1080 days. Time series of the zonal wind and vertical eddy momentum fluxes were plotted for all the runs to identify days when gravity waves might be present. Then some further 2-day integrations were done to save output every 2 hours for these periods. The output from these runs was interpolated onto a  $1.0^\circ \times 0.5^\circ$  (lat x lon) grid in the horizontal plane (Section 2.4) and later filtered using low and high-pass filters to extract wave-like behavior for further analysis.

## 2.3 Experiments



A number of experiments were performed to observe the impact on the global circulation of introducing orography in a dry GCM where gravity waves might be present. The first experiments used low resolution with a  $65 \times 32$  (lon x lat) grid. Experiments with this size grid used either uniform grid or a grid that gradually increased the resolution near the mountain, potentially allowing shorter waves to appear there that might be gravity waves. Similar simulations occurred using high resolution with a  $128 \times 64$  (lon x lat) grid.

The experiments were:

**(a) Simulations at low resolution**

(1a) The control experiment, which has a uniform grid and no orographic forcing and horizontal grid size  $5.6^\circ$  (lon) x  $5.6^\circ$  (lat) (or approximately 610 km x 610 km). The horizontal resolution is about the same as used by McFarlane (1997) in his study of parameterized gravity wave drag in a GCM.

(2a) The idealized mountain is introduced into a uniform grid that uses the same grid spacing both in the vertical and horizontal as in the control.

(3a) The grid is stretched (Fig. 2) with highest resolution at (180E, 20S). The simulation uses the same number of grid points as the control. However near (180E, 20S), the grid stretching doubles the number of grid points in the east-west direction and trebles them in the north-south direction, giving a resolution of approximately  $2.8^\circ$  (lon) x  $1.9^\circ$  (lat). Away from (180E, 20S), the latitudinal resolution becomes as low as  $9.83^\circ$  near the North Pole and  $5.91^\circ$  near the South Pole. On the opposite side of the globe in the zonal direction the grid spacing increases to  $8.83^\circ$  in longitude. The resolution varies smoothly between these extremes.

(4a) Same as in 3a, but with the mountain (Fig. 1) included.

### (b) Simulations at high resolution

Simulations at high resolution were executed at NCAR by Dr. J. Prusa with a parallel processor version of the code to reduce the overall time needed to complete simulations. All the other specifications for these experiments were the same as in the low-resolution experiments, though both runs included the mountain. The horizontal grid used 128 x 64 lon-lat grid points corresponding to a uniform  $2.8^\circ \times 2.8^\circ$  (310 x 310 km) lon-lat grid.

(1b) The vertical grid spacing was 750 m but the damping sponges were placed between 24 km and 30 km, a thickness of 6km.

(2b) The model configuration was the same as in 1(b), but horizontal grid stretching(cf. Fig. 2) was applied. Also the time step was smaller to accommodate higher resolution. Otherwise the specifications were the same as those in 1b, and the structure of the grid stretching was the same as in 3a and 4a. The finest horizontal resolution was  $0.9^\circ$  (lat) x  $1.4^\circ$  (lon) near the mountain.

### 2.4 Interpolation

For some analyses, stretched-grid results were interpolated onto a  $1.0^\circ$  (lat) x  $0.5^\circ$  (lon) grid in the xy plane using a Taylor series approximation given by

$$\begin{aligned}
 f(x_0 + h, y_0 + k) = & f(x_0, y_0) + \left( h \frac{\partial}{\partial x} + k \frac{\partial}{\partial y} \right) f(x_0, y_0) \\
 & + \frac{1}{2} \left( h^2 \frac{\partial^2}{\partial x^2} + k^2 \frac{\partial^2}{\partial y^2} + 2hk \frac{\partial}{\partial x} \frac{\partial}{\partial y} \right) f(x_0, y_0)
 \end{aligned} \tag{2.11}$$

where  $f$  is any field. We used this grid in particular to analyze the vertical wind field.

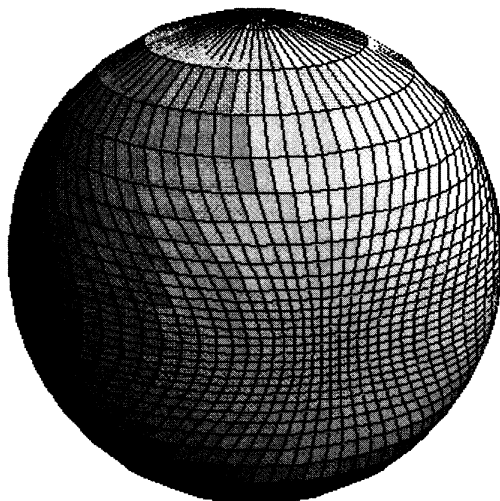


Fig. 2 Stretched grid with 65 longitudinal grid points and 32 latitudinal grid points. The grid separation is finest at (20 S, 180 E). Toward the North Pole the grid spacing is the largest. Over the Northern Hemisphere there are fewer grid points, and grid points are more concentrated in the Southern Hemisphere especially near the mountain where stretching is applied.

## 2.5 Spectral Filtering

Fourier transforms were applied to the interpolated vertical wind field to transform the field to spectral. A special filter then was applied to the  $w$  field. For coarser resolutions, longer wavelengths were retained to remove potentially erroneous and unresolved behavior at the Nyquist ‘two delta’ limit. A spectral filter was applied to the  $w$  field. The filter was applied to a 30 °-wide longitudinal zone that was selected so it can straddle the mountain. Three different filters were used, i.e. low pass, high pass and the band pass filter to search for gravity waves. The different filters are described below.

### (a) High Pass Filter

A high-pass filter retains waves above a cutoff wavenumber and attenuates those below this wavenumber. In other words it allows shorter wavelengths to pass through and attenuates longer wavelengths. The cutoff wavenumber used in this filter was 8.

**(b) Low-pass filter**

A low-pass filter retains waves below a certain cutoff wave number and attenuates waves above that number. High wavelengths are removed and low wavelengths are retained. The results from the low pass filtering did not show the gravity waves (Fig. 8).

**(c) Band-pass Filter**

A band-pass filter lies between the low-pass filter and the high-pass filter. It attenuates low wavenumbers and high wavenumbers but allows wavenumbers within the cutoff range to pass through. This filter combines low pass and high pass filters.

## CHAPTER 3

### ANALYSIS OF ZONAL WIND AND EDDY MOMENTUM FLUXES

#### 3.1 Zonal Wind and Eddy Momentum Flux Fields

In this chapter we look at the zonal wind, zonal and time averaged. Temporal and zonal averages of vertical transport and meridional transport of westerly momentum are reviewed later in the chapter for their relationship to the zonal wind through momentum convergence. This analysis helps set the stage for the analysis of gravity waves.

Convergence or divergence of vertical and horizontal eddy fluxes of westerly momentum contribute to the total change in the zonal wind (3.0):

$$\frac{\partial}{\partial t}(\rho[u]) = -\frac{\partial}{\partial y}[(\rho u)^* v^*] - \frac{\partial}{\partial z}[(\rho u)^* w^*] \quad (3.0)$$

where  $\frac{\partial}{\partial y}[(\rho u)^* v^*]$  is the divergence of eddy meridional flux of westerly momentum and

$\frac{\partial}{\partial z}[(\rho u)^* w^*]$  is divergence of eddy vertical flux of westerly momentum. Fluxes converge

when these terms are negative and contribute to increasing the zonal wind. Divergent momentum fluxes mean a decrease in the zonal wind. The term on the left hand side of the equation gives the change of zonal wind with time.

#### 3.2 Zonal Wind

Results in Table 3 were computed for each experiment by averaging zonal wind for 240 days after a 240-day spin up. Table 3 shows the magnitude, latitude and altitude of each

hemisphere's zonal jet maximum. The full width at half maximum was computed by taking half the maximum wind, noting its latitude on either side of the maximum wind, and then computing the difference between these two latitudes.

The control run (CR) of our experiments is the low-resolution (LR) run with flat terrain and uniform grid (LRUGF). In each hemisphere, a double jet structure is prominent in the CR, with a midlatitude and a polar jet (Fig. 3a). For the CR, thermal forcing is symmetric about the equator, and consequently the zonal and time averaged zonal wind is symmetric about the equator (Fig. 3a). The zonal wind has a maximum of 40 m/s at the tropopause, about 12 km from the surface, consistent with the observed annual average (Peixoto and Oort 1991). The jet also extends into the stratosphere in agreement with observations and simulation results from McFarlane (1986), though our stratosphere is idealized. The stratospheric jet is stronger than in observations.

Surface easterlies occur from the tropics to polar-regions. At the equator and areas surrounding it, light westerlies occur from about 1.5 km from surface up to the top of the stratosphere. It is also clear that the surface area covered by easterlies is larger than that covered by westerlies. There must therefore be a westerly momentum sink in the atmosphere. This may be simply the near-surface damping in our momentum forcing, but it may also be a numerical damping due to coarse resolution. The control run results otherwise show that the model reasonably simulates the atmosphere and can therefore be used for other experiments.

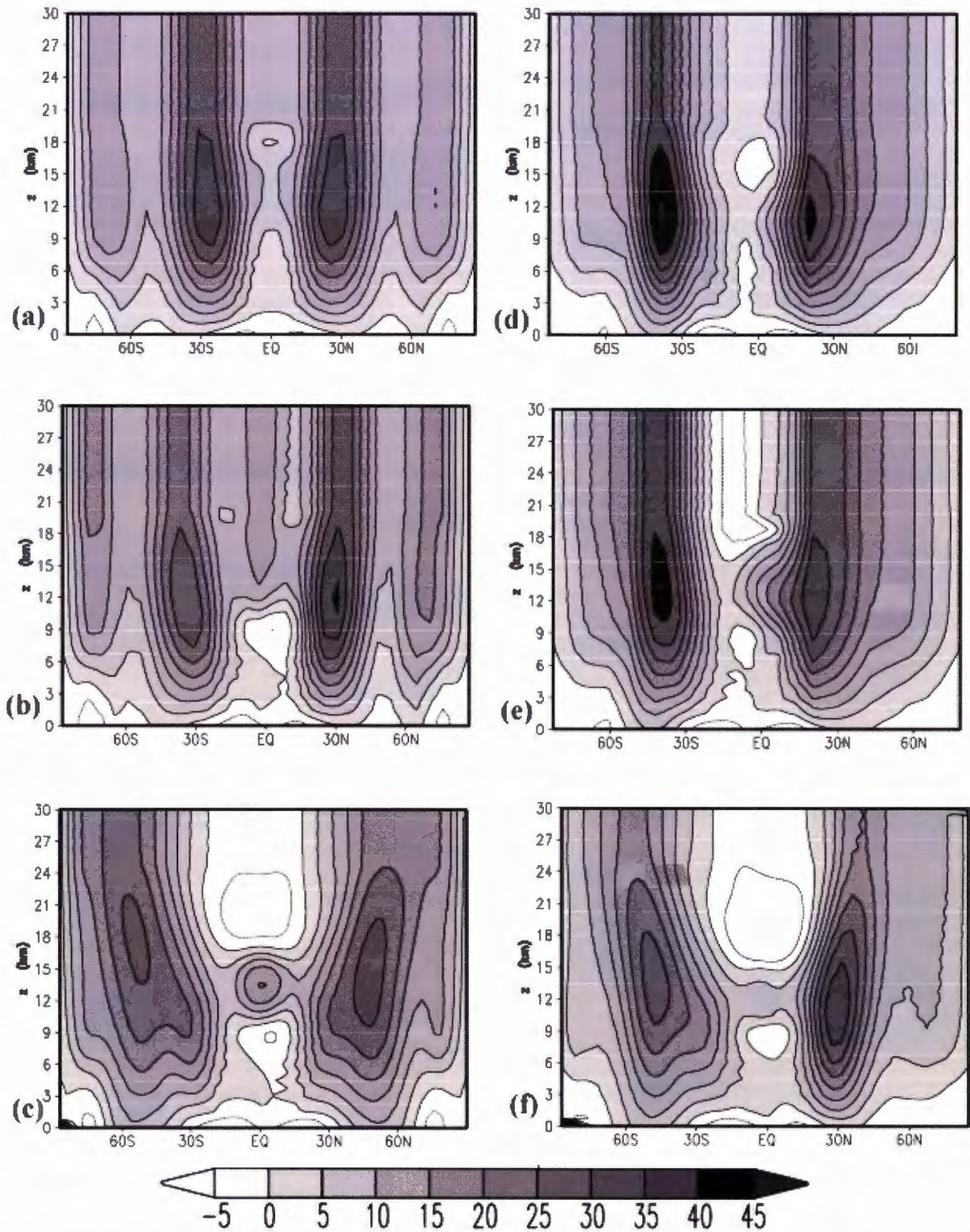


Fig. 3. Zonal/temporal averaged zonal wind for (a.) flat terrain (FT), LR and uniform grid (UG) (b.) topography, LR and UG (c.) topography, HR and UG, (d.) FT, LR and stretched grid (SG) (e.) topography, LR and SG and (f.) topography, HR and SG.

### 3.2.1 Change in Resolution

#### 3.2.1.1 Flat Terrain

We first compare the LRUGF and LRSGF runs to illustrate what grid stretching by itself does to the circulation when there are no other surface features (e.g. topography) that identify specific longitudes. Table 3 and Fig. 3 show that when Southern Hemisphere horizontal resolution is increased through our prescribed grid stretching, the height of the jet stream and maximum zonal wind speed increase and the jet shifts poleward. A possible explanation of the increase in the full width at half maximum could be the better resolution in the wind field. Also, with higher resolution, there are light easterly winds at the equator in the upper troposphere and lower stratosphere. Note that stretching the grid over the Southern Hemisphere results in reduced grid points over the Northern Hemisphere and hence a reduction in the latitudinal resolution over the same area (Fig. 2).

#### 3.2.1.2 Change in Resolution with Topography

##### (a) LRUGT vs. LRSGT

With our grid stretching and topography included, the strength of the jet increases ( $9 \text{ ms}^{-1}$ ) over the Southern Hemisphere and increases by a small amount in the Northern Hemisphere compared to the run with uniform grid and no mountain. The Southern Hemisphere latitudinal shift in the jet maximum is poleward as occurred when topography was added (Table 3 and Fig. 3); nonetheless the jet shifts equatorward in the Northern Hemisphere. Similarly, the altitude of the jet increases which also occurred for the topography versus flat terrain comparison (Section 3.2.1.1). On the other hand the full width at half maximum increases by a large margin ( $17^\circ$ ) (Table 3) in the Northern Hemisphere and less in the Southern Hemisphere when the Southern Hemisphere grid resolution is increased.



### **(b) HRUGT vs. HRS GT**

We see a pattern similar to that in the previous cases of change in resolution, though the maximum zonal wind increases more in the Northern Hemisphere than in the Southern Hemisphere. The latitudinal shift is opposite to that in the LR cases, and is equatorward in both hemispheres though more so in the Northern Hemisphere. Increasing the grid resolution over the Southern Hemisphere at higher resolution causes the jet to shift towards the equator (Fig. 3).

Generally, imposing grid-stretching yields stronger zonal jet maxima in both hemispheres. Also grid stretching causes the primary jets in both hemispheres to become wider and shift poleward and upward in the Southern Hemisphere for the LR cases, but has an opposite effect on the latitudinal shift in the Northern Hemisphere. For the HR cases stretching causes the opposite behavior to that seen in the Southern Hemisphere for the LR cases. It is important to note that grid stretching in the LR with topography cases causes the width of the jet to decrease in the Southern Hemisphere.

### **(c) LRUGT vs. HRUGT**

Comparison between LR and HR shows changes opposite to cases in which resolution is increased through grid stretching. Here increasing the resolution results in a small decrease of about 1.0 m/s in the maximum zonal wind over the Southern Hemisphere and a much bigger decrease of approximately by 8.0 m/s over the Northern Hemisphere (Table 3). There is a poleward shift in the jet maxima and the altitude of the jet and the full width at half maximum increases in both hemispheres and is much bigger in the Southern Hemisphere (6 km).

#### **(d) LRSGT vs. HRSGT**

Increasing resolution throughout the domain with topography present causes a large decrease in the maximum zonal wind over the Southern Hemisphere (9 m/s). However, over the Northern Hemisphere the maximum zonal wind only increases slightly (2.0 m/s). The jet maximum shifts equatorward in both hemispheres as the resolution increases.

When resolution is increased everywhere the maximum zonal wind decreases more in the SG cases compared to the UG cases in the Southern Hemisphere. Increasing resolution has an opposite effect in the Northern Hemisphere where it yields a large decrease in the maximum wind for the UG cases and a slight increase for the SG cases.

### **3.2.2 Change in Topography**

Addition of a mountain distorts the symmetry in the mean zonal wind (Fig. 3b). There is a poleward shift in the jet maximum for both hemispheres when topography is included (Table 3).

#### **(a) LRUG (F vs. T)**

When orography is included in the model, the maximum zonal wind in the Southern Hemisphere decreases by about 20% compared to the flat terrain scenario. However the maximum wind in the Northern Hemisphere changes very little.

#### **(b) LRSG (F vs. T)**

Unlike the uniform grid case, when terrain is included the maximum zonal wind decreases by the same amount (8 %) in both hemispheres.

Southern Hemisphere maximum wind decreases with addition of orography for the two cases. Also, adding the “Andes” range causes the full width at half maximum to decrease

Table 3. Latitude, height, maximum speed and full width half maximum for the different experiments.

Southern Hemisphere				
Experiment	Maximum Speed (m/s)	Latitude ( ° )	Height (km)	Full width at half maximum ( ° )
LRUGF	41	25	10	25
LRS GF	46	38	11	28
LRUGT	33	37	12	31
LRS GT	42	38	14	26
HRUGT	32	55	18	44
HRS GT	33	48	14	36
Northern Hemisphere				
Experiment	Maximum Speed (m/s)	Latitude ( ° )	Height (km)	Full width at half maximum ( ° )
LRUGF	40	25	10	26
LRS GF	42	20	11	32
LRUGT	40	31	12	25
LRS GT	40	20	13	42
HRUGT	32	50	15	42
HRS GT	42	31	11	24

by a small amount in the Northern Hemisphere compared to the Southern Hemisphere where it increases by 10°.

In general the LR runs with a mountain in them showed a very sharp change in the zonal wind from the level where the absorbers start to the top of our idealized atmosphere, showing possible reflection by the sponges. The reflection is not very sharp for the LR runs with uniform grid. Absorbers for the HRUGT run were very strong, thus a sharp change in the zonal flow can be seen at 24 km above the surface. However, the absorbers for the HRS GT run were much weaker since there is no sharp change in the zonal flow.

Table 4. Maximum meridional flux of zonal momentum and its position (latitude and height) for the Northern and Southern Hemisphere.

Southern Hemisphere			
Experiment	Minimum flux ( $\text{kg}\cdot\text{m}^{-1}\cdot\text{s}^{-2}$ )	Latitude ( $^{\circ}$ )	Height (km)
LRUGF	-19.1	19.7	6.0
LRS GF	-25.7	30.6	6.75
LRUGT	-24.5	19.7	6.0
LRS GT	-26.6	32.8	6.0
MRUGT	-31.9	35.2	6.0
MRS GT	-32.98	34.2	6.0
Northern Hemisphere			
Experiment	Maximum flux ( $\text{kg}\cdot\text{m}^{-1}\cdot\text{s}^{-2}$ )	Latitude ( $^{\circ}$ )	Height (km)
LRUGF	17.2	19.7	6.0
LRS GF	26.8 (25)	12.6 (20)	4.5 (6.0)
LRUGT	18.3	19.7	6.0
LRS GT	29.2	12.6	4.5
MRUGT	36.1	35.0	6.0
MRS GT	21.1	23.7	6.0

LRUGF has a bimodal northern hemisphere jet; the characteristics of the second jet are in parenthesis.

### 3.2 Eddy Meridional Flux of Westerly Momentum $[(\rho u)^* v^*]$

In general, centers of maximum flux convergence of westerly momentum coincide with areas of maximum zonal velocity as can be seen in Fig. 5 and Fig. 4.

#### 3.2.1 Flat Terrain and LR

Fig. 4 shows the distribution of the meridional transport of westerly momentum by the eddies, which is related to the maintenance of the zonal mean wind distribution through (3.0). In the LRUGF run (low resolution, uniform grid and flat topography), the mean meridional flux of zonal momentum is anti-symmetric about the equator (Fig. 4a) and transports westerly momentum poleward. In the Southern Hemisphere, the maximum flux is

above  $25 \text{ kg-m}^{-1}\text{-s}^{-2}$ , whereas in the Northern Hemisphere it lies between  $15 \text{ kg-m}^{-1}\text{-s}^{-2}$  and  $20 \text{ kg-m}^{-1}\text{-s}^{-2}$ . The differences in the amplitude of the fluxes can be attributed to numerical errors or the relatively short averaging period. The centers of maximum flux in the tropics are far from observed climatology.

In Fig. 4d the momentum structure is more organized on the largest scales and there are two distinct centers of maximum poleward horizontal flux of momentum, just as in climatology (Oort and Peixoto, 1992), though the centers do not coincide with those in climatology, which are located in the midlatitudes. For the stretched grid, one center in the Southern Hemisphere is at  $30^\circ \text{ S}$  and the one in the Northern Hemisphere lies in the tropics. The momentum flux is slightly more intense than in the previous situation but weaker than climatology. Low-resolution runs with no terrain do not produce meridional structures like observed. Zonal wind maxima occur within areas of convergence in the horizontal momentum fluxes (Fig. 3a, Fig. 3d, Fig. 4a and Fig. 4d). Thus, zonal wind is partly maintained by meridional transport of westerly momentum.

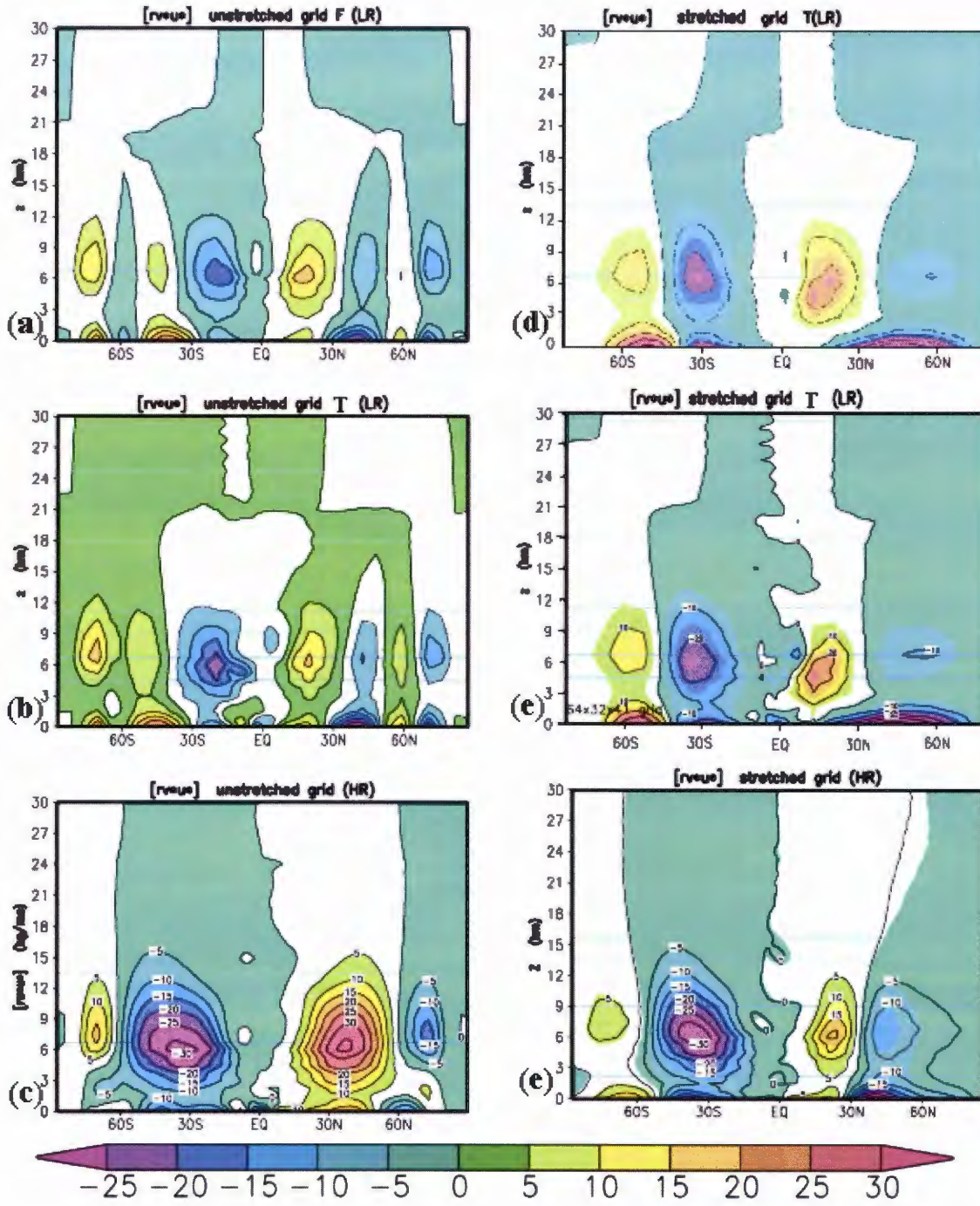


Fig. 4. The eddy meridional transport of horizontal momentum for (a.) flat terrain (FT), LR and uniform grid (UG), (b.) topography, LR and UG, (c.) topography, HR and UG, (d.) FT, LR and stretched grid (SG), (e.) topography, LR and SG and (f.) topography, HR and stretched grid.

### 3.3.2 Terrain and LR

It is interesting to note that including topography had very little effect on the positions of maximum momentum flux, though the eddy meridional flux in westerly momentum is slightly stronger than in the CR in the tropical and polar regions of the Southern Hemisphere. There is very little change in the strength of the meridional flux in the Northern Hemisphere compared to the CR except for an increase in the magnitude of the flux near 60°N.

Places of maximum convergence and divergence of the meridional flux of westerly momentum are very similar to the CR. However stretching of the grid for the LRS GT run results in a more intense flux in momentum (Fig. 4e), and there are only two regions of maximum momentum flux, just as in the LRSGF case. The only difference between the LRS GT and LRSGF cases is the position of the convergence and divergence of the meridional fluxes of westerly momentum. There is a southward shift for the divergence in the equatorial region. Places of convergence do not shift in the extra-tropical regions of both hemispheres. Including of a mountain and grid stretching positioned the area of convergence in the midlatitudes in the Southern Hemisphere and northward of 30°N in the Northern Hemisphere, in agreement with position of the jet maxima near 25°N and 35°S. This is close to observed climatology (Peixoto and Oort 1992).

### 3.3.3 Terrain and HR.

Compared to LR cases, at higher resolution, we see an increase in the latitudinal extent of momentum fluxes of the same sign and a large increase in the momentum maximum in the Southern Hemisphere's tropics. Fig. 4c shows a symmetrical structure about the equator in the mean meridional flux of momentum for the run with uniform grid with

topography at high resolution (HRUGT). A region of maximum momentum flux convergence occurs near the 60° latitude and slightly poleward of the jet maximum for each hemisphere. The position of the maximum flux of meridional momentum in the midlatitudes is in agreement with climatology (Peixoto and Oort, 1992). On the stretched grid, the area of maximum momentum flux convergence shifts by almost 30° compared to the HRUGT case in the Northern Hemisphere (Fig. 4f), but in the Southern Hemisphere there is no change in the position of the maximum flux convergence of westerly momentum. Another important feature to note is the shrinking and reduction in the strength of the flux of momentum relative to uniform grid case at HR in the Northern Hemisphere, consistent with the narrow jet in the Northern Hemisphere (Fig. 3d). Consequently the convergence around 30°N for the stretched HR grid is much weaker than the convergence for the unstretched grid. The area of momentum convergence corresponds with the jet maximum in the Northern Hemisphere. Divergence in the momentum occurs at about 5°N, consistent with the weak wind field in that area.

### 3.4 Eddy Vertical Flux of Westerly Momentum $[(\rho u)^* w^*]$

#### 3.4.1 Flat Terrain and LR

Fig. 5 shows time and zonal average eddy vertical transport of westerly momentum. Fig. 5a does not show any extrema throughout the globe that are as large as in other cases. This suggests poor resolution in the vertical flux of westerly momentum. Horizontal resolution for our model (6.25 °) is slightly larger than width of our mountain. Finer resolution is needed for realistic simulation of the vertical momentum fluxes that are



presumably generated by gravity waves. The vertical flux of westerly momentum is symmetric about the equator, consistent with the zonal average zonal wind,  $[u]$  (Fig. 3a). The maxima of vertical flux convergence of westerly momentum coincide with areas of maximum  $[u]$ . When the grid is stretched (Fig. 5d), the maxima in the zonal wind become stronger. One is centered near  $30^\circ$  S and the other is close to  $20^\circ$  N. These zonal wind maxima in each hemisphere are in regions of vertical flux convergence. It can be seen that with increased resolution in the Southern Hemisphere, the eddy vertical flux of westerly momentum in both hemispheres becomes stronger, especially in the Southern Hemisphere.

### 3.4.2 Terrain and LR

In the Southern Hemisphere, with a uniform grid and topography included, the vertical flux has positive and negative extrema (Fig. 5b), whereas the Northern Hemisphere has only a weak maximum. The presence of the mountain may be causing the positive/negative structure in the Southern Hemisphere. As the resolution in the Southern Hemisphere increases through grid stretching (Fig 5e.), a center of maximum vertical flux of momentum emerges in the Northern Hemisphere tropics, and the positive/negative pair that we saw in the Southern Hemisphere for the uniform grid still exists. However the positive structure is broader and deeper and the negative structure has weakened. The positive/negative structure almost coincides with the area of convergence of horizontal flux of momentum and zonal velocity. Note that, near the surface, in the Southern Hemisphere's tropics, there is an upward flux of zonal momentum. The meridional structures appear to be better simulated when the resolution increases.

### 3.4.3 Terrain and HR

The vertical flux of westerly momentum has a positive/negative pair of maxima in the tropics for the uniform and stretched grid cases (Fig. 5c and 5f). The area downward flux in the tropics troposphere coincides with the region of easterly flow at 9 km. For the unstretched grid case, the fluxes are stronger in the Northern Hemisphere and slightly weaker over the mountain (Fig. 5c). However when resolution is increased through grid stretching, vertical flux decreases in the Northern Hemisphere and increases in the Southern Hemisphere. Also the center of maximum flux becomes narrower in the Northern Hemisphere, consistent with a narrower jet in same hemisphere (Fig. 3f).

As resolution increases in the Southern Hemisphere, eddy momentum flux decreases in the Northern hemisphere due to the reduced resolution in the Northern Hemisphere. The positive/negative structure in southern tropics is smaller and weaker with increased resolution (Fig. 5c and 5f).

The lowest resolution ( $5.625^\circ \times 5.625^\circ$ ) resolves poorly the meridional structure to of the vertical flux field. Stretched grids and HR grids, however, resolve the meridional structures well as evidenced by the distinct extrema in the vertical flux field and the consistent flux structure for these cases. For the stretched grids, the Northern Hemisphere extrema are weaker compared to their Southern Hemisphere counterparts, consistent with decline in the resolution in the Northern Hemisphere. Westerly momentum is transported upwards and polewards from the tropics to the poles in both hemispheres (Fig. 5c and 5f).

Table 5. Maximum vertical flux of westerly momentum and its position (latitude and height) for the Northern and Southern Hemisphere.

Southern Hemisphere			
Experiment	Maximum flux ( $\text{kg}\cdot\text{m}^{-1}\cdot\text{s}^{-2}$ )	Latitude ( $^{\circ}$ )	Height (km)
LRUGF	0.0182	19.7	6.8
LRS GF	0.044	28.5	6.0
	0.044	26.6	4.5
LRUGT	0.039	8.4	6.0
LRS GT	0.061	28.5	3.8
HRUGT	0.045	32.4	4.5
HRS GT	0.051	29.9	4.5
Northern Hemisphere			
Experiment	Maximum flux ( $\text{kg}\cdot\text{m}^{-1}\cdot\text{s}^{-2}$ )	Latitude ( $^{\circ}$ )	Height (km)
LRUGF	0.0178	19.7	6.0
LRS GF	0.038	20.2	6.8
LRUGT	0.011	36.6	3.8
LRS GT	0.038	20.2	6.8
HRUGT	0.057	32.2	6.0
HRS GT	0.028	20.4	4.5

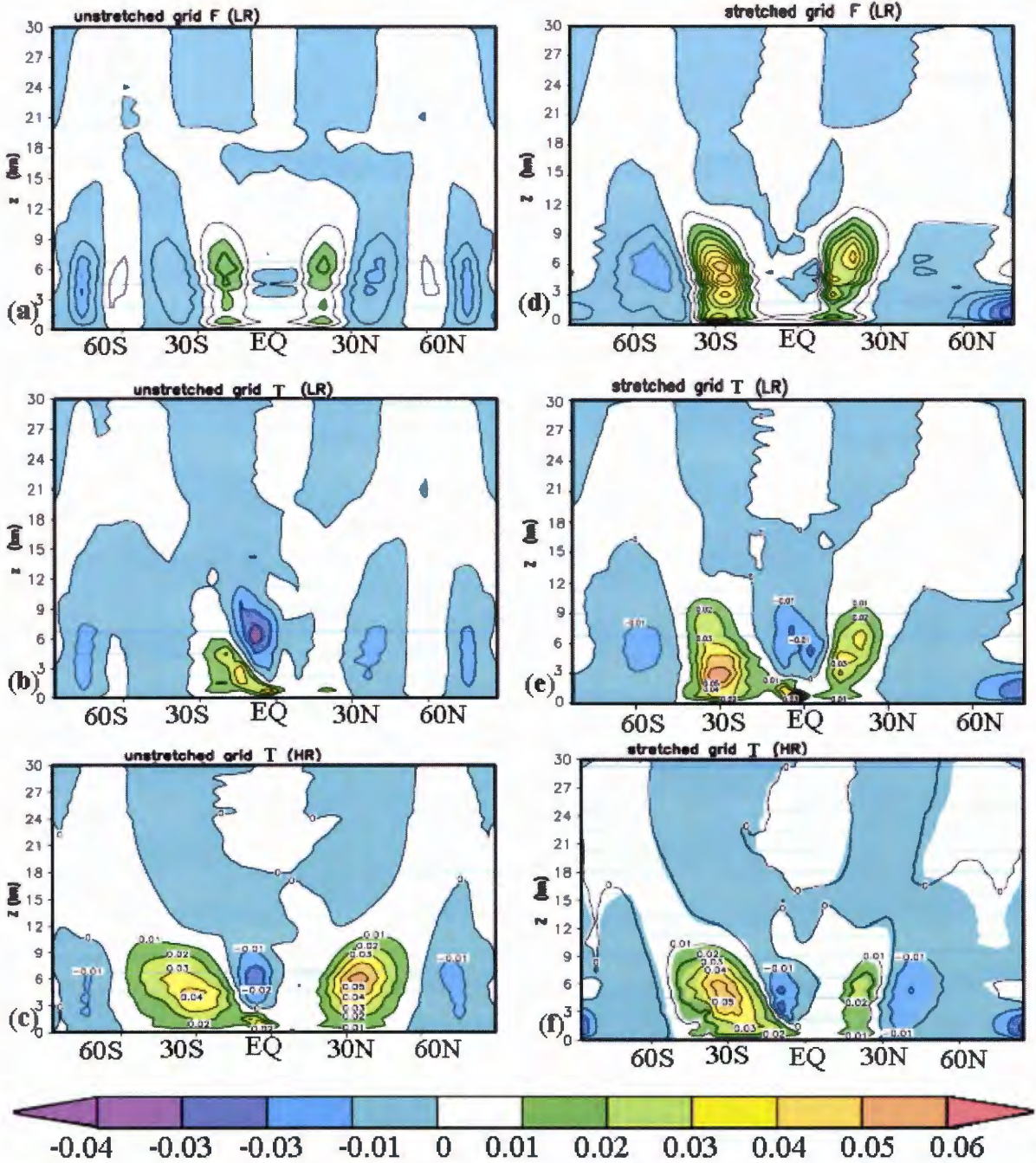


Fig. 5 Zonal/temporal averaged eddy vertical transport of westerly momentum for (a.) flat terrain (FT), LR and uniform grid (UG) (b.) topography, LR and UG (c.) topography, HR and UG, (d.) FT, LR and stretched grid (SG) (e.) topography, LR and SG and (f.) topography, HR and SG.

Table 6. Behavior of the horizontal eddy flux of westerly momentum, when the resolution is changed.

	Maximum [ $\rho v' u'$ ]		Resolution		Latitude		Height	
Hemisphere	SH	NH	SH	NH	SH	NH	SH	NH
LRUGF-LRSGF	I (35)	I (56)	I	D	P	EQ	I	D
LRUGT-LRSGT	I (66)	I (-36)	I	D	P	EQ	C	D
LRUGT-HRUGT	I (30)	I (97)	I	I	P	P	C	C
HRUGT-HRSGT	I (3)	D (-42)	I	D	EQ	EQ	C	C
LRSGT-HRSGT	I (24)	D (28)	I	I	P	P	C	I

Table 7. Behavior of the vertical eddy flux of westerly momentum when the resolution is changed.

	Maximum [ $\rho w' u'$ ]		Resolution		Latitude		Height	
Hemisphere	SH	NH	SH	NH	SH	NH	SH	NH
LRUGF-LRSGF	I (144)	I (111)	I	D	P	P	D	I
LRUGT-LRSGT	I (56)	I (245)	I	D	P	EQ	D	I
LRUGT-HRUGT	I (15)	I (418)	I	I	P	EQ	D	I
HRUGT-HRSGT	I (13)	D (-51)	I	D	EQ	EQ	C	D
LRSGT-HRSGT	D (-26)	D (-16)	I	I	P	P	I	D

I denotes an increase, D decrease, P poleward, EQ denotes equatorward and C represents constant SH and NH denote Southern Hemisphere and Northern Hemisphere respectively. The numbers in parenthesis are percentage increases when resolution is increased through grid stretching or increasing the number of grid points.

Fluxes shift poleward in the Southern Hemisphere and equatorward in the Northern Hemisphere for the topography simulations with the exception of the HR runs, where the shift is equatorward in both hemispheres (Table 6 and Table 7). The flux convergences follow the zonal wind maxima.

## CHAPTER 4

### ANALYSIS OF GRAVITY WAVES

#### 4.1 Introduction

Earlier we stated that one of the possible causes of gravity wave development is stratified air flowing over terrain. The mountain in our study is idealized for the development of gravity waves. We shall see that in our simulations, gravity waves were resolved at the highest resolution in the model,  $1.4^\circ$  (lon)  $\times$   $0.9^\circ$  (lat), and that lower resolutions were not adequate to resolve gravity waves. In this chapter, we analyze waves that were generated by our model using the vertical wind field that has been filtered to focus on possible gravity-wave behavior. This is achieved by looking at the wind field to see if waves have the structure and phase speed given by linear theory and by looking at very high-resolution, two-dimensional simulations. The regional-simulation data and longitudinal averaged data for the vertical wind were obtained from Dr J. Prusa through private communication.

#### 4.2 Searching for Gravity Waves

Gravity waves transport momentum, and therefore we expect them to change the zonal wind of their environment. We extracted time series of zonal average zonal wind and vertical eddy flux of westerly momentum  $[(\rho u)^* w^*]$  to identify periods when there could possibly be gravity wave activity (Fig. 6). Temporal standard deviations of these fields were

computed, and we selected points of maximum temporal standard deviation to examine further the time series. Maximum temporal standard deviation might occur where the gravity wave is growing and possibly developing, changing the zonal wind. The time series were plotted for a period of 240 days after the spin-up time. These were then used to obtain targeted time periods to look for the gravity-wave structures. Periods when the momentum flux was large (Fig. 7a) or zonal wind was changing rapidly (Fig. 7b) were selected because we assumed that these behaviors might indicate episodes of strong gravity-wave momentum flux convergence or divergence. After the targeted periods were selected, the model was re-run for these periods for two days, and the vertical velocity field was saved every hour. Latitude and longitude cross-sections (Fig. 8) of vertical wind were then made at 5.25 km altitude (above the mountain but close to the source) to search for wave-like behavior. Fig 8a shows the x-y cross-section of the vertical wind field interpolated onto a uniform grid for the HRSGT run, and Fig 8b is for the LRSGT run. Fig. 8c (LRUGT) shows very little wavelike behavior. Wavelike behavior in the east-west direction is more prominent in the HRSGT run. Latitude-height cross-sections of  $w'$  were made after the wave-like behavior had been established, where  $w'$  is the departure from the time average of the targeted time period.



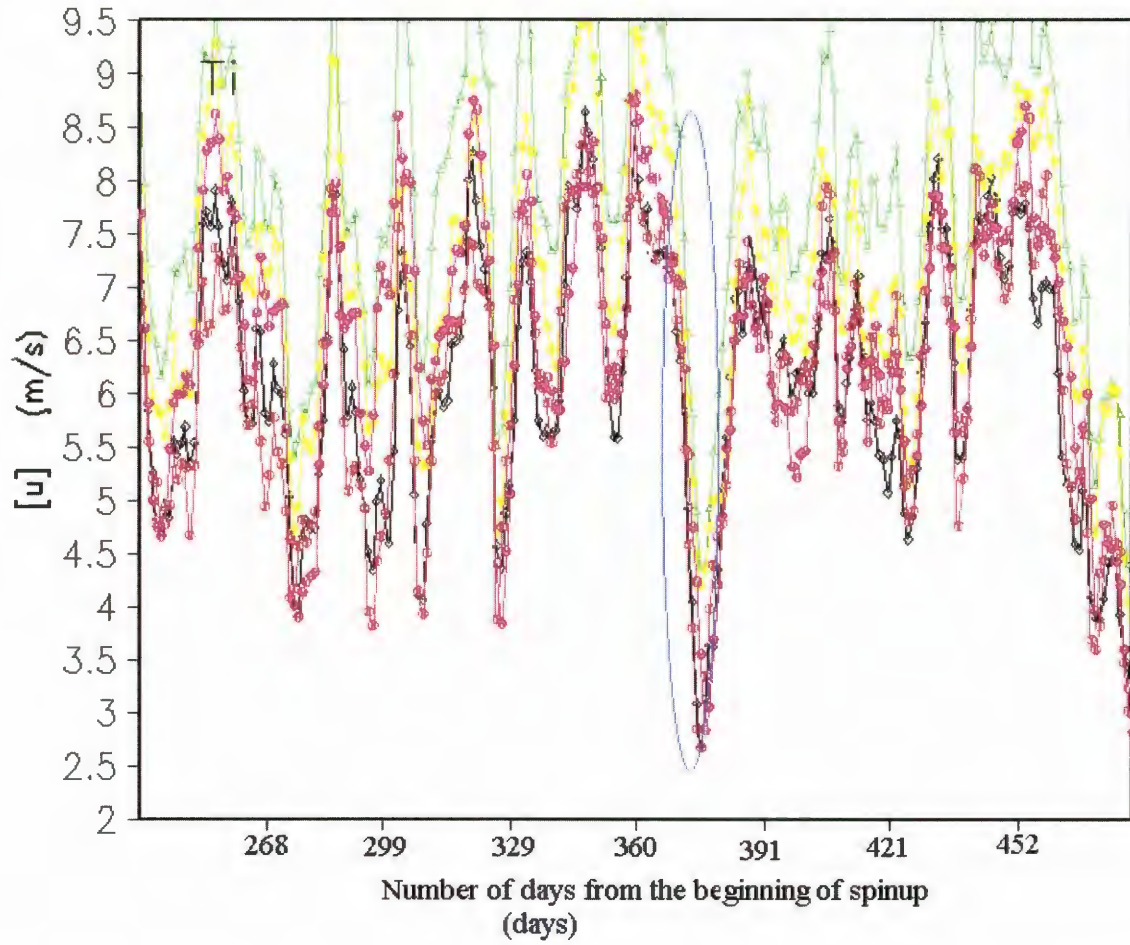


Fig. 6 The time series for the zonal and time averaged zonal wind  $[u]$  (m/s) for unstretched grid at HR. The plot is for the first 240 days after the spinup. The time series plotted use the latitudes and height coordinates  $(-14.4^\circ, 5.25 \text{ km})$ ,  $(-14.4^\circ, 6 \text{ km})$ ,  $(-14.4^\circ, 6.75 \text{ km})$ ,  $(-15.8^\circ, 6 \text{ km})$  and  $(-13.0^\circ, 6 \text{ km})$ .  $[u]$  is changing rapidly from day 365 to day 380 of the simulation (the circled region). The different curves are not identified because we are searching for common behavior.



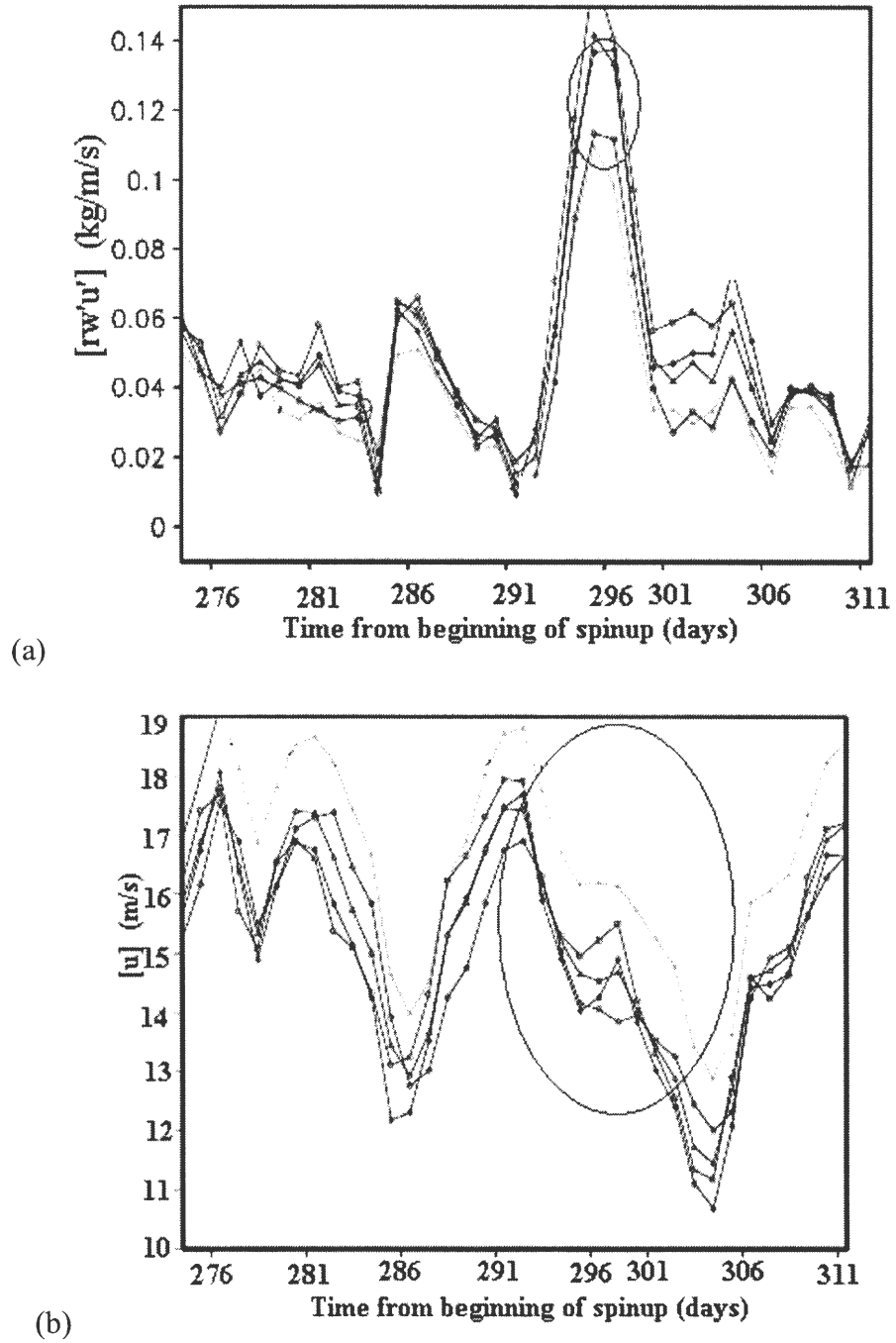


Fig. 7 The time series for the zonal and time average of simulated (a)  $[(\rho u)^* w^*]$  ( $\text{kg}\cdot\text{m}^{-1}\cdot\text{s}^{-2}$ ) and (b) zonal wind  $[u]$  ( $\text{m/s}$ ) for the targeted period for a stretched grid simulation at high resolution. The latitudes and height coordinates used in the diagram are  $(-29.9^\circ, 5.25 \text{ km})$ ,  $(-29.9^\circ, 6 \text{ km})$ ,  $(-29.9^\circ, 6.75 \text{ km})$ ,  $(-28.5^\circ, 6 \text{ km})$  and  $(-27.1^\circ, 6 \text{ km})$ . The circle shows in (a) maximum flux and in (b) regions in which  $[u]$  is changing rapidly. Individual curves were not labeled because we were looking for common behavior.

#### 4.2.1 Tools for searching for gravity waves

Tools that were used to search for gravity waves were described in more detail in Chapter 2. Two methods were used in the search for gravity waves. First the model output of vertical motion ( $w$ ) for the targeted time periods was interpolated onto a  $0.5^\circ$  (lat)  $\times$   $1.0^\circ$  (lon) grid for all runs, as described in Section 2.4. Spectral filtering for  $w$ , constructed using Fourier transforms was applied near the mountain. A band-pass filter removed waves with wave numbers outside the band 4 to 8, (wavenumbers are defined in terms of a  $30^\circ$  longitudinal zone about the mountain). Other wavenumber bands were also tested, such as 6-10 and 8-12. For LR and uniform HR output, other local wavenumber bands were used (e.g. 1-3, 5-7) to avoid “two delta” noise at the limit of original, uninterpolated grid resolution. The wavenumber band was chosen because apparent gravity waves were clearly resolved in that band. Results for a stretched grid at HR showed better-resolved gravity wave activity compared to the other results. For a uniform grid at HR the model behavior shows resemblance to under-resolved waves, i.e. the resolution is too low to resolve the gravity waves. The waves are evanescent in the vertical for all LR results (Fig. 9a) and uniform grid results at HR (Fig. 9b). Evanescence is more pronounced in the LR plot. The results with the HR stretched grid show that resolution at least this fine is required to begin to resolve the gravity waves produced here (Fig. 10). This figure shows an x-z cross-section of vertical wind for local wavenumbers 4-8. More results are shown in Fig. 11 and Fig. 12. In Fig. 11 and Fig. 12 there are about three waves in the  $30^\circ$ -longitude band and the waves tilt westward with height. A distinct wavelike behavior appears on the leeward side of the mountain, suggesting that the gravity waves formed on the leeward side of the mountain.

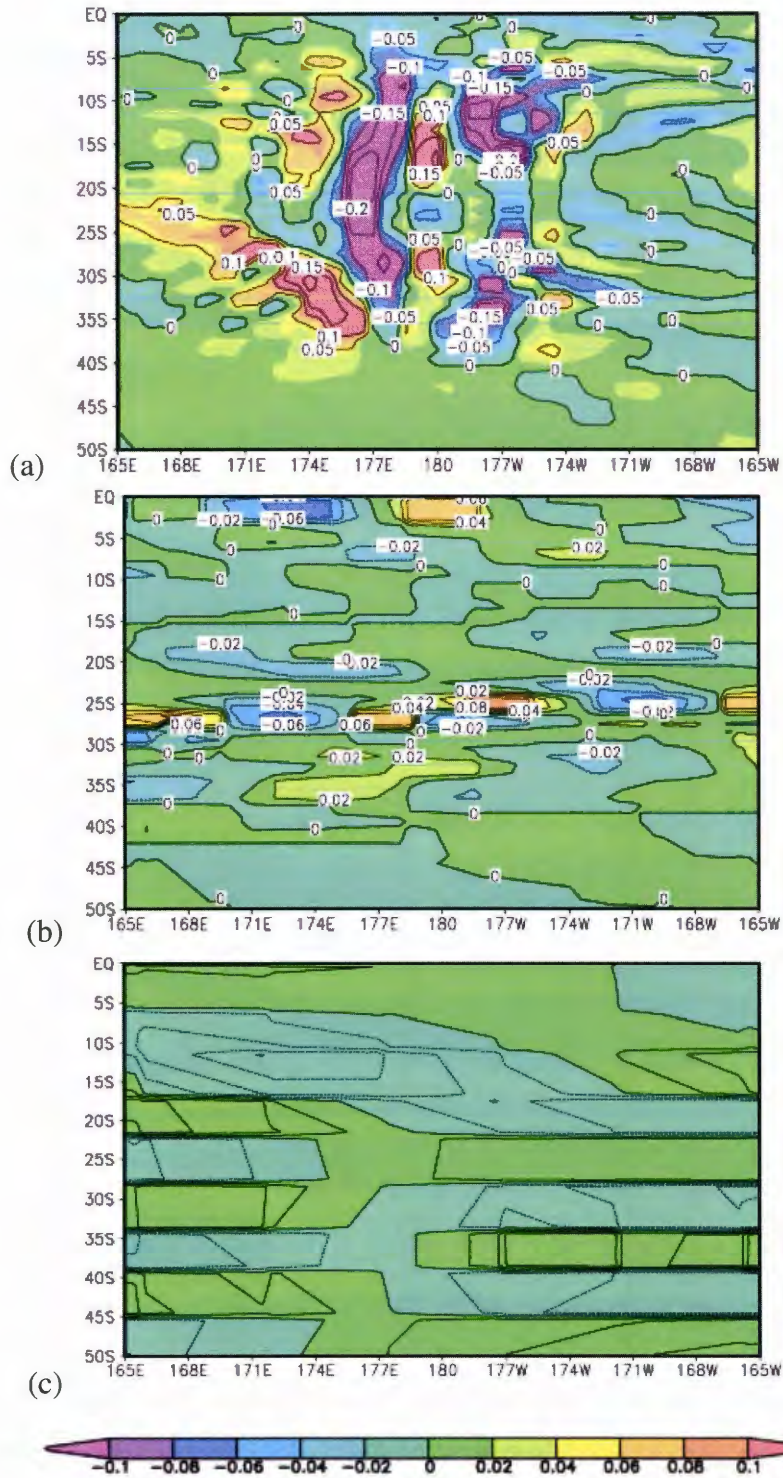


Fig. 8 Band pass filtered xy cross-section of the unfiltered vertical velocity at 5.25 km above the ground for (a) a stretched grid at HR, 298 days after spin-up, (b) stretched grid at LR, 318 days after spin-up, and (c) the unstretched grid at LR, 311 days and 6 hr after spin-up.

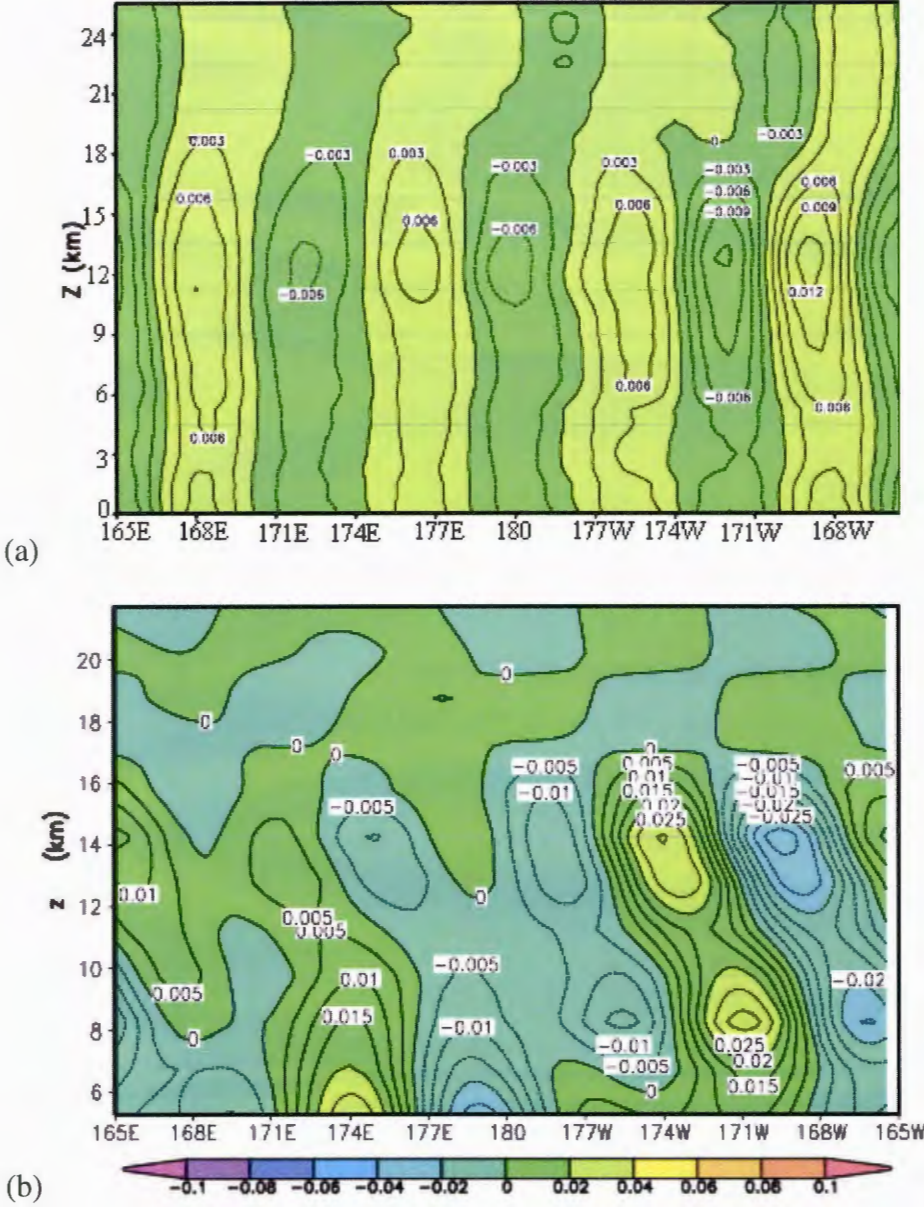


Fig. 9 Band-pass filtered longitude-height cross-section of vertical wind perturbation ( $w'$ ) (a) for LR stretched grid run with topography at  $t=317$  days 15 hr, wavenumbers 4-8, (b) for HR uniform grid simulation at  $t=298$  days 19 hr.

We also passed the interpolated output through low-pass, high-pass and band-pass filters for the LR and HR runs with topography. Gravity waves were more apparent in the band-pass filtered results compared to the other two results.



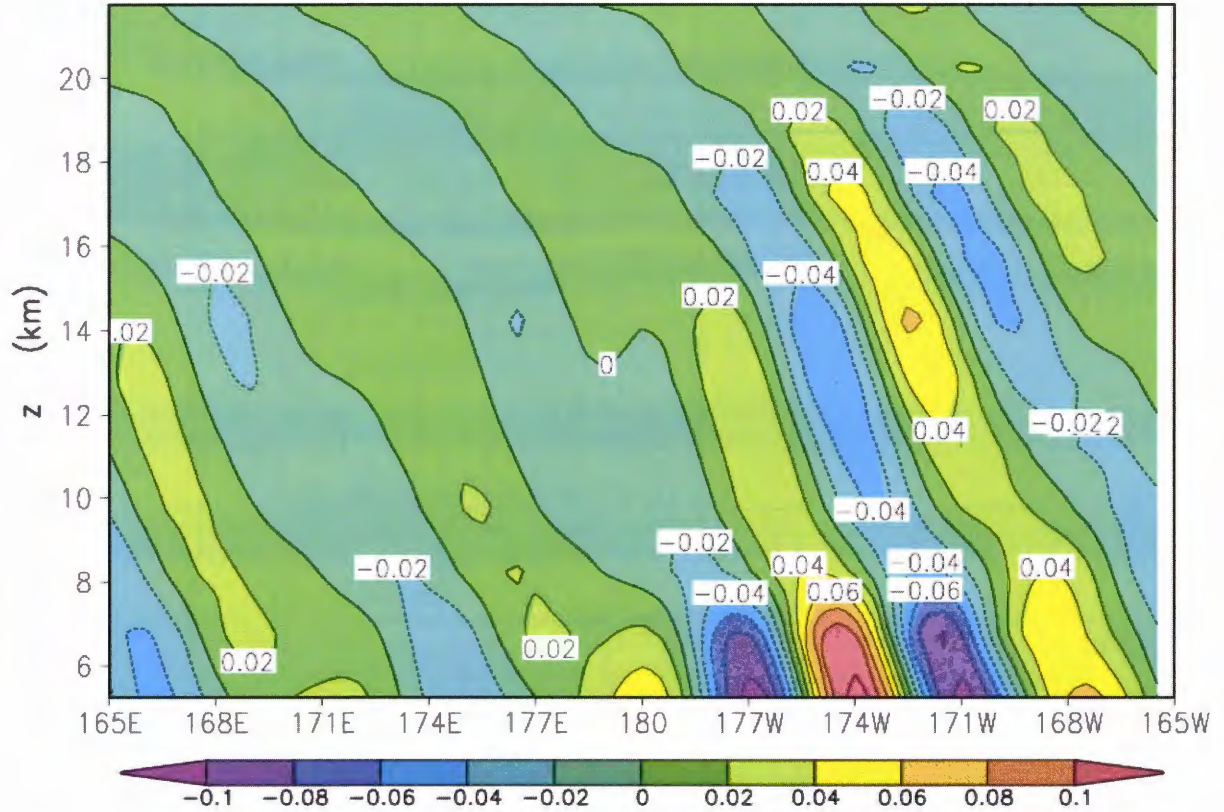


Fig. 10 Longitude-height cross-section of vertical wind perturbation ( $w'$ ) 298 days after spin up. The wind field  $w$  is passed through a band-pass filter that passed local wavenumbers 4-8.

### 4.3 Simulated Wave Properties

The waves in Fig. 11 and 12 were selected for analysis because they showed two distinct wave regimes: the first group occurred in the first 16 hours after the start of the targeted period (297 hrs) and the second group occurred between 37 and 48 hours after the start of the targeted period. The first group of waves shows a stationary wave changing in amplitude slightly. In the second group of waves, the stationary wave is more pronounced with larger amplitude. This wave is growing with time and more rapidly in the last six hours of the simulation.

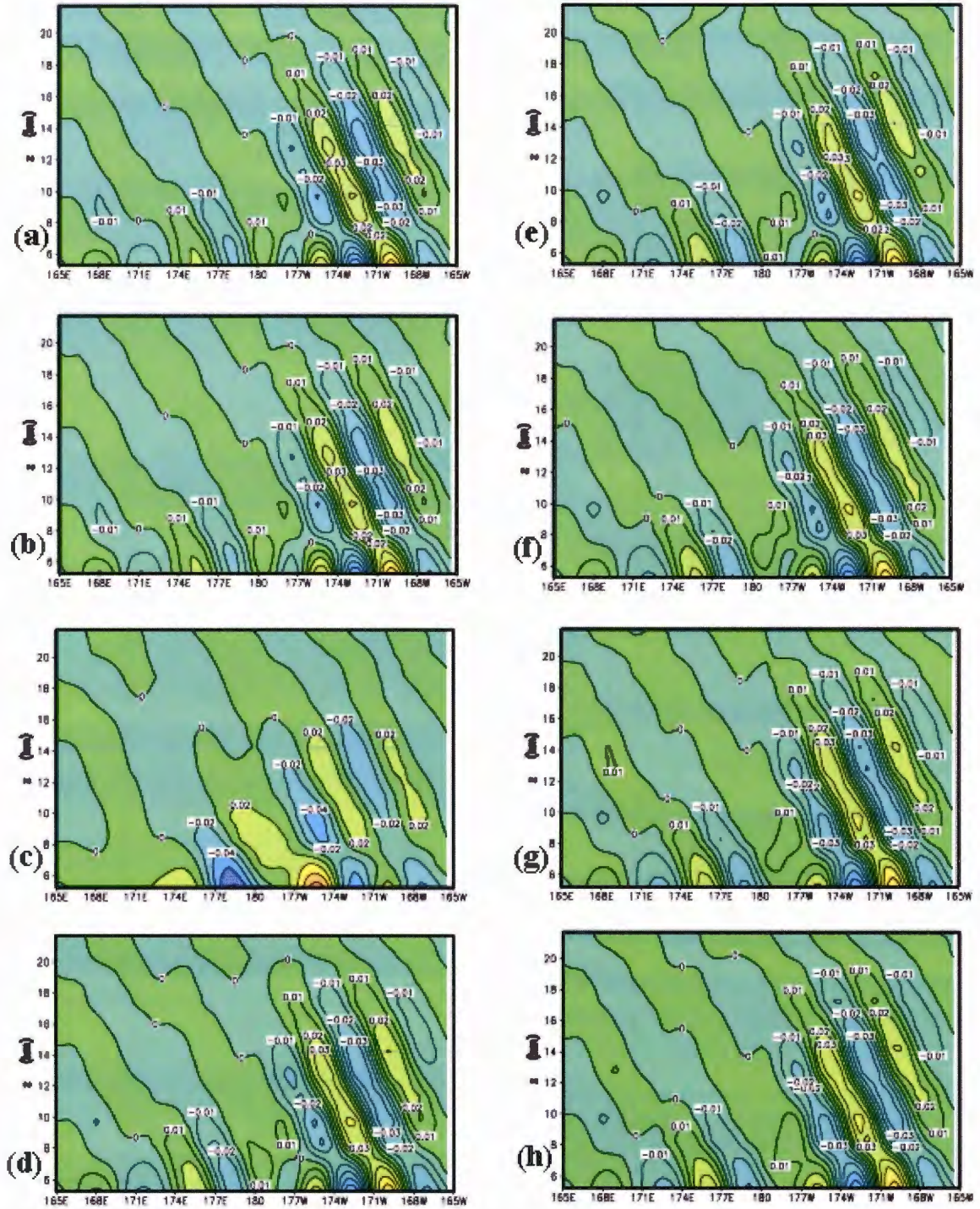


Fig.11 Longitude-height cross-section of 4-8 wavenumber band-pass filtered vertical wind perturbation  $w'$ . Spectral filtering was applied to  $w$  for the  $30^\circ$ -longitude band from  $165^\circ$  E to  $165^\circ$  W. Cross-sections are shown for the periods 297 days plus (a) 1 hr, (b) 2hr, (c) 3 hr, (d) 4 hr, (e) 5 hr, (f) 6 hr, (g) 7 hr, (h) 8 hr, (i) 9 hr, (j) 10 hr, (k) 11 hr, (l) 12 hr, (m) 13 hr, (n) 14 hr, (o) 15hr and (p) 16 hr for HR stretched grid simulations.



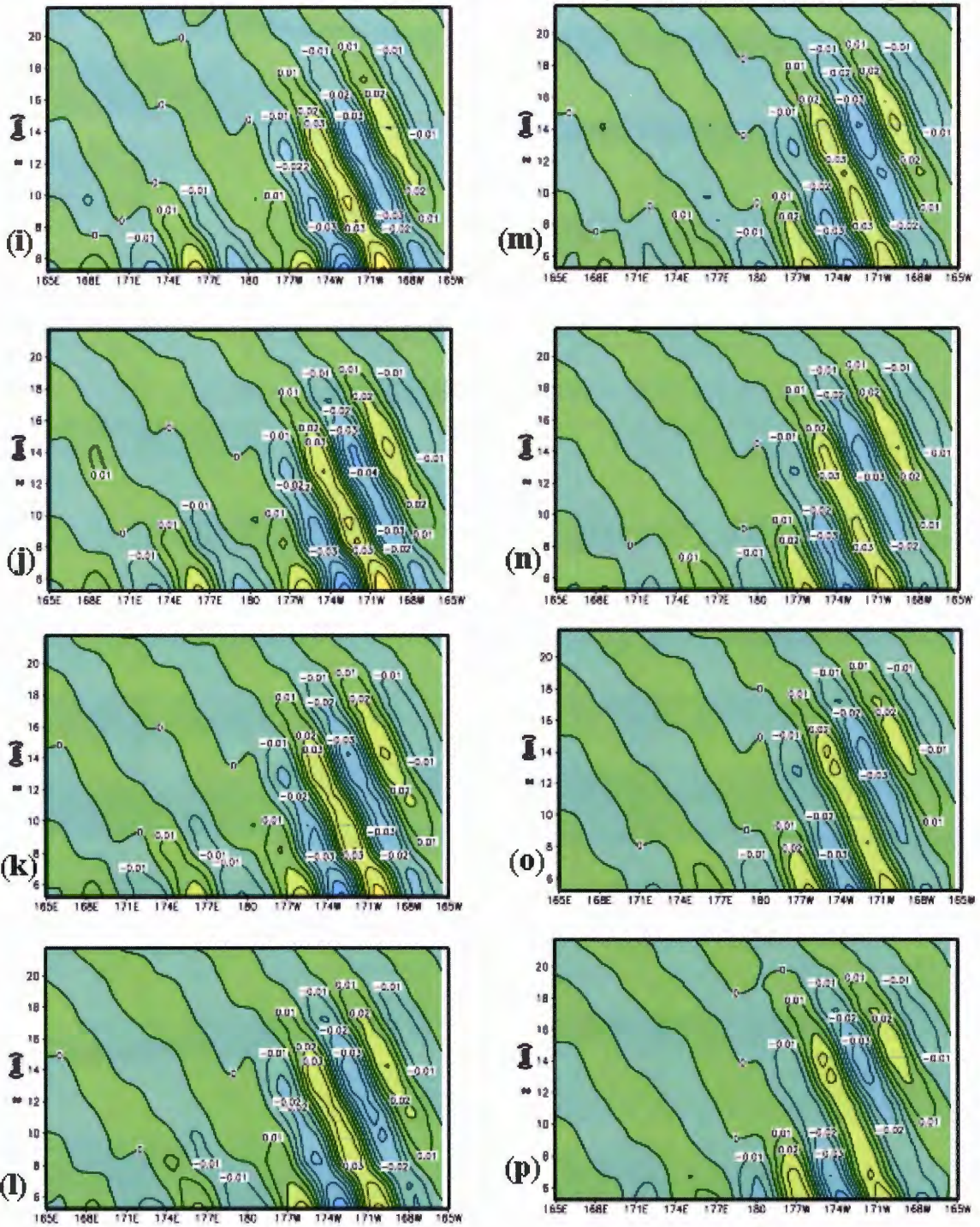


Fig.11 (continued)



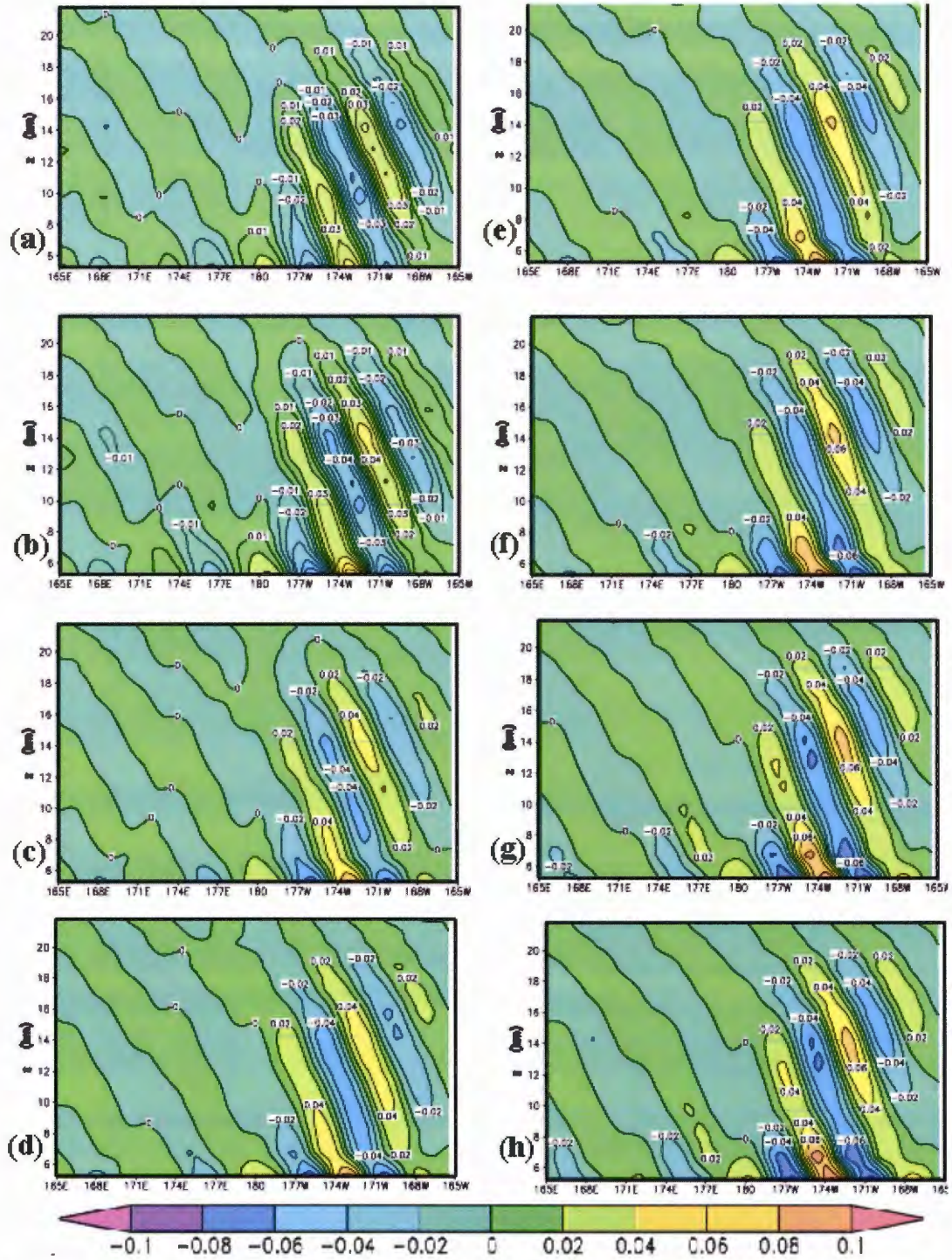


Fig.12 Longitude-height cross-section of vertical wind perturbation  $w'$ , for day 299 plus (a) 13 hr, (b) 14 hr, (c) 15 hr, (d) 16 hr, (e) 17 hr, (f) 18 hr, (g) 19 hr, (h) 20 hr, (i) 21 hr, (j) 22 hr, (k) 23 hr, and (l) day 300 at HR with a stretched grid. The wavenumber band is 4-8; waves outside this range are filtered out. Spectral filtering was applied to  $w$  for the  $30^\circ$  longitude band from 165 E to 165 W.



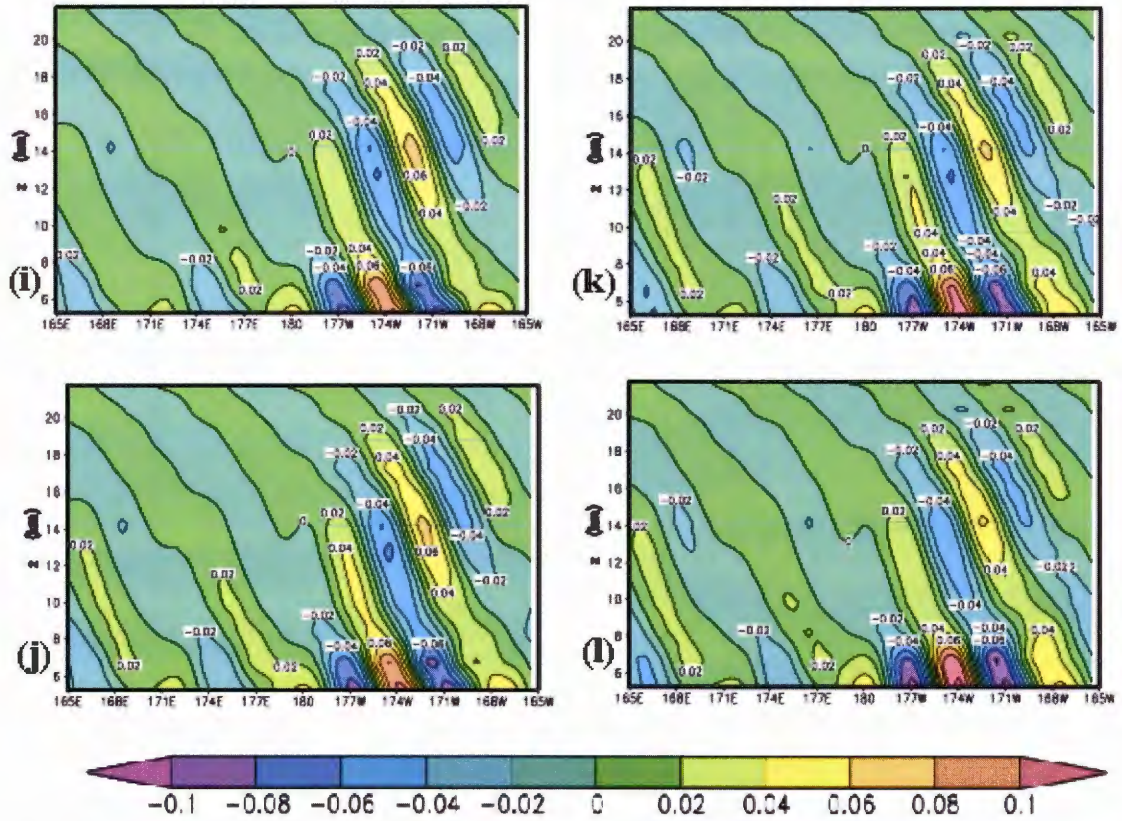


Fig.12 (continued)

These two figures were used to explore the gravity wave properties such as the vertical and horizontal wavelengths and the phase speeds for the two regimes. They were similar to Keller's (1983) image showing wave trapping properties of non-hydrostatic waves. Note that our images start at 5.25 km altitude.

#### 4.3. 1 Wave Regimes

##### (a) Regime 1

The phase speeds (Table 9) were estimated by following the motion of one phase line at a given altitude over a 15-hour period. The phase speed was measured at two points: 5.25 km

(close to the mountain) and 15 km altitude (further from the mountaintop). The waves closer to the mountain had speeds 5 times faster than those at 15 km. Horizontal wavelengths were estimated by drawing lines along troughs and crests and measuring the resulting distance between the two at constant altitude for the 1<sup>st</sup> and 16<sup>th</sup> hour (Table 10). For each time, the wavelength was measured at 3 locations (altitudes) and an average wavelength was computed for the three altitudes. The combined results gave  $\lambda_x = 5.8 \pm 0.3^\circ = 525 \pm 30$  km. The difference between the wavelengths for the two times was 25 km, which was not statically significant (J. Prusa, personal communication).

The vertical wavelengths were estimated by drawing lines along crests and troughs and measuring vertical distance along lines of constant longitude. We chose longitudes close to the mountain, where gravity waves were more active (Table 11). Five points were used to measure the wavelengths for the two times. The difference between the two populations was statistically significant at 10 km but not so at 15 km (J. Prusa, personal communication).

The average wavelength at time 1 hour (9.2 km) is statistically different from that at 16 hours (11.4 km). The waves were growing with time. Twenty-eight hours after the start of the targeted period, transition waves occurred between 5.25 and 8 km altitude. These had a horizontal wavelength of 455 km and a vertical wavelength of 22 km. Their horizontal wavelength was slightly shorter than that for the Regime 1 waves though the vertical wavelength was almost twice that of the Regime 1 waves.

### **(b) Regime 2**

For this regime of waves the phase speeds (Table 12) were estimated by following the motion of particular phase lines at a given altitude for a period of 11 hrs. The difference between the two populations was statistically significant (J. Prusa, personal communication).

The procedure for measuring horizontal and vertical wavelengths was the same as that used for Regime 1 waves, and the measurements were done at time 37 and 48 hours after the start of the targeted period. The difference between the two populations was not statistically significant (J. Prusa, personal communication). The combined wavelength for the two populations at 37 and 48 hours was  $\lambda_x = 5.8 \pm 0.3^\circ = 530 \pm 20 \text{ km}$ .

The differences between the two populations for the vertical wavelengths both for times (37 and 48 hours) and altitudes (10 vs. 15 km) were not statistically significant (J. Prusa, personal communication).

Table 9 Regime 1 Horizontal Phase Speeds for time=1-16 hrs

Feature	Z (kms)	x (long.)	$c_x$ (deg/hr)	$c_x$ (m/s)	
1	5.25	173W	-0.063		
2	5.25	176W	-0.087		
<b>Average phase speed</b>			<b>-0.075±0.02</b>	<b>-1.9±0.5</b>	<b>Low Alt. Synopsis</b>
3	15	173W	+0.010		
4	15	176W	+0.023		
<b>Average phase speed</b>			<b>+0.017±0.01</b>	<b>+0.4±0.3</b>	<b>Hi Alt. Synopsis</b>

Table 10 Regime 1 Horizontal Wavelengths for time1 & 16 hrs

Time (hrs)	z (kms)	$\lambda_x$ (deg)	$\lambda_x$ (km)	
1	5.25	5.3		
1	10	5.6		
1	15	6.0		
<b>Average wavelength for layer 10-15 km</b>		<b>5.65±0.35</b>	<b>515±30</b>	<b>1 hr. Synopsis</b>
16	5.25	6.2		
16	10	5.95		
16	15	5.65		
<b>Average wavelength for layer 10-15 km</b>		<b>5.9±0.3</b>	<b>540±25</b>	<b>16 hr. Synopsis</b>

Table 11 Regime 1 Vertical Wavelengths for times 1 &amp; 16 hrs

Time (hrs)	x (deg)	ave z (km)	$\lambda_z$ (km)	
1	170W	10	9.3	
1	173W	10	9.2	
1	177W	10	9.2	
1	177W	15	10.6±0.6	
Average wavelength for layer 10-15 km		10	9.2±0.1	1 hr. Synopsis
16	170W	10	11.0	
16	173W	10	11.3	
16	177W	10	12.0	
16	177W	15	10.4±0.3	
Average wavelength for layer 10-15 km		10	11.4±0.5	16 hr. Synopsis

Table 12. Regime 2 Horizontal Phase Speeds: 37-48 hrs

Feature	z (kms)	x (long.)	$c_x$ (deg/hr)	$c_x$ (m/s)	
5	5.25	173.5W	-0.082		
6	5.25	176.5W	-0.082		
Average phase speed			-0.082±0.0	-2.1±0.	Low Alt. Synopsis
7	15	172.5W	-0.045		
8	15	175W	-0.032		
Average phase speed			-0.039±0.01	-1.0±0.25	Hi Alt. Synopsis

Table 13 Regime 2 Horizontal Wavelengths for time t=37 &amp; 48 hrs

Time (hrs)	z (kms)	$\lambda_x$ (deg)	$\lambda_x$ (km)	
37	5.25	5.8		
37	10	5.7		
37	15	5.4		
Average wavelength		5.65±0.2	515±20	37 hr. Synopsis
48	5.25	5.9		
48	10	6.05		
48	15	6.05		
Average wavelength		6.0±0.1	545±10	48 hr. Synopsis

Table 14 Regime 2 Vertical Wavelengths: 37 &amp; 48 hrs

Time (hrs)	x (deg)	ave z (km)	$\lambda_z$ (km)	
37	170W	10	10.7	
37	173W	10	10.7	
37	177W	10	11.5	
37	177W	15	10.8	
<b>Average wavelength</b>		<b>10</b>	<b>11.0±0.5</b>	<b>37 hr. Synopsis</b>
48	170W	10	11.7	
48	173W	10	11.1	
48	177W	10	11.3	
48	177W	15	11.1	
<b>Average wavelength</b>		<b>10</b>	<b>11.4±0.3</b>	<b>48 hr. Synopsis</b>

The average horizontal wavelength for the two regimes was  $530 \pm 25$  km, the vertical wavelength was  $11.1 \pm 0.5$  km and the horizontal wave speed was  $0.5 \pm 1.0$  m/s. These values were used later in a dispersion relationship to test for consistency..

#### 4.3.2 Zonal averaged wind fields

Our analysis required the average environment near the mountain. We generated zonal average parameters by taking an average over a  $30^\circ$  longitude band centered on the mountain for a prescribed set of latitudes. One such parameter was the zonally averaged zonal wind. It was averaged over the 48 hours used in the wave analysis. Fig. 14 shows three profiles, corresponding to using:

1. only  $-35.73^\circ$  (averaging in x only).
2. a  $3.0^\circ$  latitude band centered about  $-35^\circ$  (averaging in x and y)
3. and a  $6.0^\circ$  latitude band centered about  $-35^\circ$  (averaging in x and y).

Larger latitude bands were not used because of changes in the topography and coriolis parameter. The profiles match very well and show a uniform vertical wind shear of

$1.69 \times 10^{-3} \text{ s}^{-1}$  from the surface to an altitude of 14 km. The profile shows a maximum wind of 24.5 m/s at 14.0 km. Zonal, temporal averages of meridional wind (not shown) are about three times smaller, allowing us to assume in further analysis that meridional wind  $v = 0$ .

#### 4.4 Dispersion Relationship

We assess the properties of the simulated waves with respect to linear gravity waves to see if the simulated waves are consistent with gravity-wave behavior. One can derive a dispersion relationship for gravity waves (J. Prusa, personal communication) to determine their behavior in the environments simulated for this project. We can then use this behavior to see if the simulated waves correspond to the gravity waves given by linear theory. We assume a basic state in hydrostatic equilibrium, which can be represented by the following expressions:

$$\partial p_o / \partial z = -\rho_o g \quad (4.0)$$

$$p_o = \rho_o R T_o \quad (4.1)$$

$$\theta_o = T_o (p_{ref} / p_o)^\kappa \quad (4.2)$$

If the potential temperature  $\theta_o(z)$  is known, then the other three variables can be determined from the three equations above. We assume the basic state for a perturbation wave equation represented by  $\rho_o(z), p_o(z), T_o(z)$  and  $\theta_o(z), \theta_e(z) = \theta_o(1 + \bar{h}(z)), \rho_o(z) = \rho_{oo} \exp(-z/H_\theta)$  where

$$\theta_o(z) = \theta_{oo} \exp(z/H_\theta) \quad (4.3)$$

$p = p_{oo}$  at the surface and  $H_\theta$  is the potential temperature scale height. Reference pressure was carefully selected such that the corresponding value of  $T_{oo}$  results in an acceptable value of surface density given by

$$\begin{aligned}\rho_{oo} &= p_{oo} / (RT_{oo}) \\ &= p_{ref} / (R\theta_{oo})(p_{ref} / p_{oo})^{\kappa-1}\end{aligned}\quad (4.4)$$

In general,  $T_{oo} \neq \theta_o$  and the reference pressure is not necessarily equal to the surface pressure.

Pressure and density are four-dimensional dependent variables that vary with (t, x, y and z) and are expanded as  $\xi = \xi + \xi''$ . When substituted into the full f-plane model equations they yield:

$$\frac{du}{dt} = fv \sin \phi - fw \cos \phi - \frac{\partial p''^*}{\partial x} \quad (\text{east/ west momentum}) \quad (4.5)$$

$$\frac{dv}{dt} = -fu \sin \phi - fw \cos \phi - \frac{\partial p''^*}{\partial y} \quad (\text{north/ south momentum}) \quad (4.6)$$

$$\frac{dw}{dt} = fu \cos \phi - \frac{\partial p''^*}{\partial z} + g \frac{\theta'}{\theta_o} \quad (\text{vertical - momentum}) \quad (4.7)$$

$$\frac{d\theta}{dt} = 0 \quad (\text{energy}) \quad (4.8)$$

$$\frac{\partial u}{\partial x} + \frac{\partial v}{\partial y} + \frac{1}{\rho_o} \frac{\partial(\rho_o w)}{\partial z} = 0 \quad (\text{continuity}) \quad (4.9)$$

where  $\theta' = \theta - \theta_e$ ,  $\theta_e(y, z)$  is a prescribed environmental profile (ideally from a sounding)

that provides the reference state for buoyancy force and  $p''^* = p'' / \rho_o$  is a normalized

perturbation pressure. The anelastic equations above provide a full representation of the full

model equations provided perturbation terms satisfy conditions such as  $\rho' / \rho_o \ll 1$  and the

vertical wave number of dynamical motions satisfies  $\ell \gg 1/H_\theta$ , where  $\ell$  is the vertical wave number.

#### 4.4.1 Perturbation equations

The wave is represented by  $\xi = \bar{\xi} + \xi'''$  and we assume a basic state represented by  $(\bar{u}, \bar{v}, \bar{w}) = (\bar{u}, 0, 0)$ ,  $\theta(z) = \theta_o(z) \exp(z/H_\theta)$ ,  $\theta_e(z) = \theta(1 + \bar{h}(z))$  and  $\rho(z) = \rho_o \exp(-z/H_\rho)$ . Substituting these into (4.5 – 4.9) and dropping all the quadratic terms, we get our perturbation equations (not shown).

All perturbations variables are represented by a wave propagating in three dimensions with the form

$$\xi''' = \Xi \exp(zL_\xi) \Psi(t, x, y, z)$$

where  $\Xi$  is a constant,  $\exp(zL_\xi)$  is a secular growth term with inverse scale height  $L_\xi$ ,  $\Psi = \exp[i(kx + my + lz) - \omega t]$  and  $i^2 = -1$ . We require  $L_\xi$  to be the same for all variables so that the secular terms arising from our wave form balance. Furthermore, we assume that basic state zonal wind  $\bar{u}(z)$ , potential temperature deviation  $\bar{h}(z)$  and the scale heights  $H_\rho$  and  $H_\theta$  are replaced by constants representing local-average values  $[\bar{u}]$ ,  $[\bar{h}]$ ,  $[\bar{H}_\rho]$  and  $[\bar{H}_\theta]$ , so that the resulting equations are only locally valid.

The wave equation is substituted in the perturbation equations, giving five equations from which a 5x5 matrix is formed. The existence of non-trivial solutions requires that the determinant of that matrix equal zero, from which a complex equation with complex solution for  $\omega$  given  $k$ ,  $m$  and  $l$ , is obtained. After simplifying this expression we get a quadratic



expression for the general gravity wave dispersion relationship (J. Prusa, personal communication):

$$\left( K^2 + \frac{1}{4[H_\rho]^2} \right) OM^2 - \left( \frac{f_c k}{[H_\rho]} \right) OM - \left[ (f_s l + f_c m)^2 + \frac{f_s^2}{4[H_\rho]^2} + g(k^2 + m^2) \left( \frac{1 + [\bar{h}]}{[H_\theta]} \right) \right] = 0 \quad (4.10)$$

where  $OM = \omega - k[\bar{u}]$  is the Doppler shifted, or relative, frequency,  $f_c = f \cos \phi$  and  $f_s = f \sin \phi$ . To simplify (4.10) we assume the environmental and basic state potential temperature are the same i.e.  $[\bar{h}] = 0$ . From this it follows then  $g/[H_\theta] = [N]^2$  where  $[N]$  is the local Brunt-Vaisala frequency given by

$$N^2 = \frac{g}{\theta_o} \frac{\partial \theta_o}{\partial z} \quad (4.11)$$

In our case, we use geometric mean values of parameters (Table 15) for the layer 8-17 km because the wind shear is uniform in this band. This is the same layer for which the vertical and horizontal wavelengths for the waves in our HRS GT case were measured. The simulated Brunt-Vaisala frequency for this layer at 35°S was  $1.218 \text{ s}^{-2}$ .

#### (a) Case One: Stationary Waves

We assume that our waves are stationary, consistent with the behavior in Fig.12, so that  $\omega=0$  in (4.10), and also assume  $\lambda_x = 530 \text{ km}$ . The other parameters for this case are in Table 15, and when substituted into (4.10) they yield  $Lz = \pm 11.5 \text{ km}$ . The measured value

of vertical wavelength in Fig.12 is  $11.1 \pm 0.5$  km. The value from the simulation thus deviates from the value needed for stationary waves in the linear relationship by only a small amount [a difference of  $(0.5/11.1) \times 100 = 5\%$ ].

### (b) Case Two: Transient Waves

In this second case we assume  $\lambda_z$  and  $\lambda_x$  based on values from the simulation, and then we use the dispersion (4.10) to predict  $\omega$ . The value of the physically realistic frequency from the dispersion relationship is  $7.59 \times 10^{-6} \text{ s}^{-1}$  or a period of about 230 hrs. The wave speed was computed from  $c_x = \omega / k$ , giving a phase speed of 0.64 m/s. This is close to the measured wave speed of  $-0.5 \pm 1.0$  m/s.

Cases One and Two show consistency between the measured wave properties and the linear theory of gravity waves, since the measured properties fit well with our dispersion equation (4.10). The wave speed in Case Two is very small, so that our assumption in Case One that the waves are quasi-stationary is consistent.

Table 15 Parameters used to check the consistency in the dispersion relationship(4.12)

Case	Parameter	$[\bar{h}]$	$[H_\rho]$ (km)	$H_\theta$ (km)	$[u]$ (m/s)	$L_w$ (km)	$\lambda_x$ (km)	$\lambda_z$ (km)
1	Value	0.125	6.25	98.1	20.5 (SIM)	12.5	530	11.1 (SIM) 11.5 (DR)
2	Value	0.125	6.25	98.1	20.5 (SIM)	12.5	530	11.1(SIM)

SIM denotes the simulated value and DR denotes value derived from dispersion relationship.

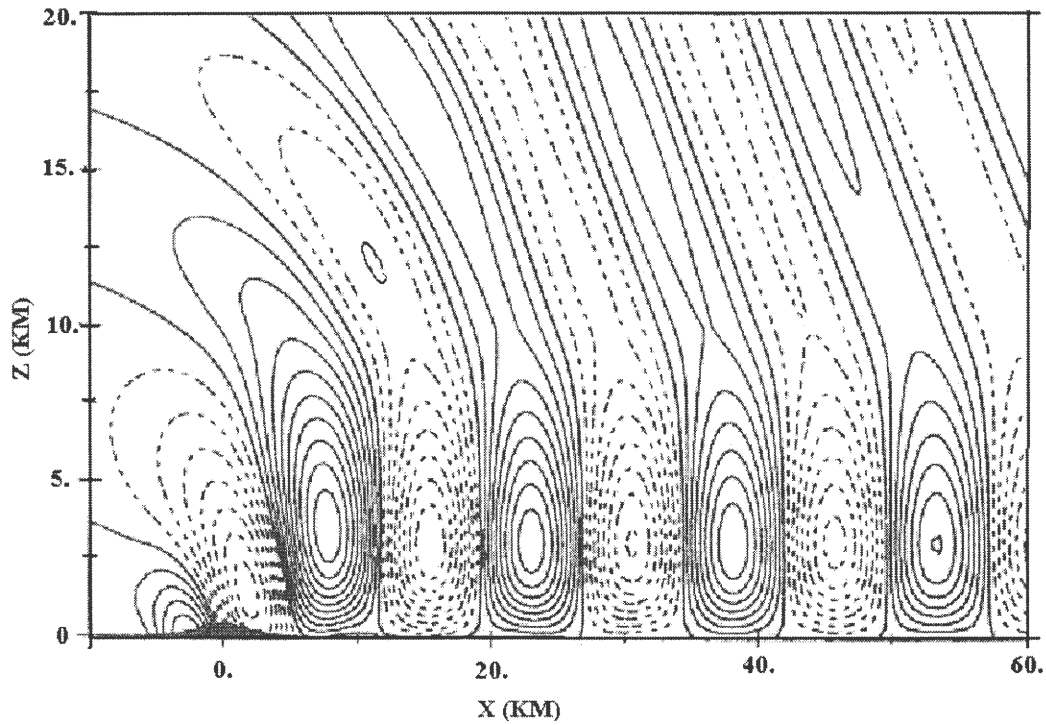


Fig. 13 Nonhydrostatic solution for the troposphere-stratosphere model by Keller (1983) Displayed are contours of vertical velocity with a contour interval of  $0.2 \text{ ms}^{-1}$ .

■ U profile at -35.73 (1), -35.75 (3.00), -35.80 (6.03) deg.

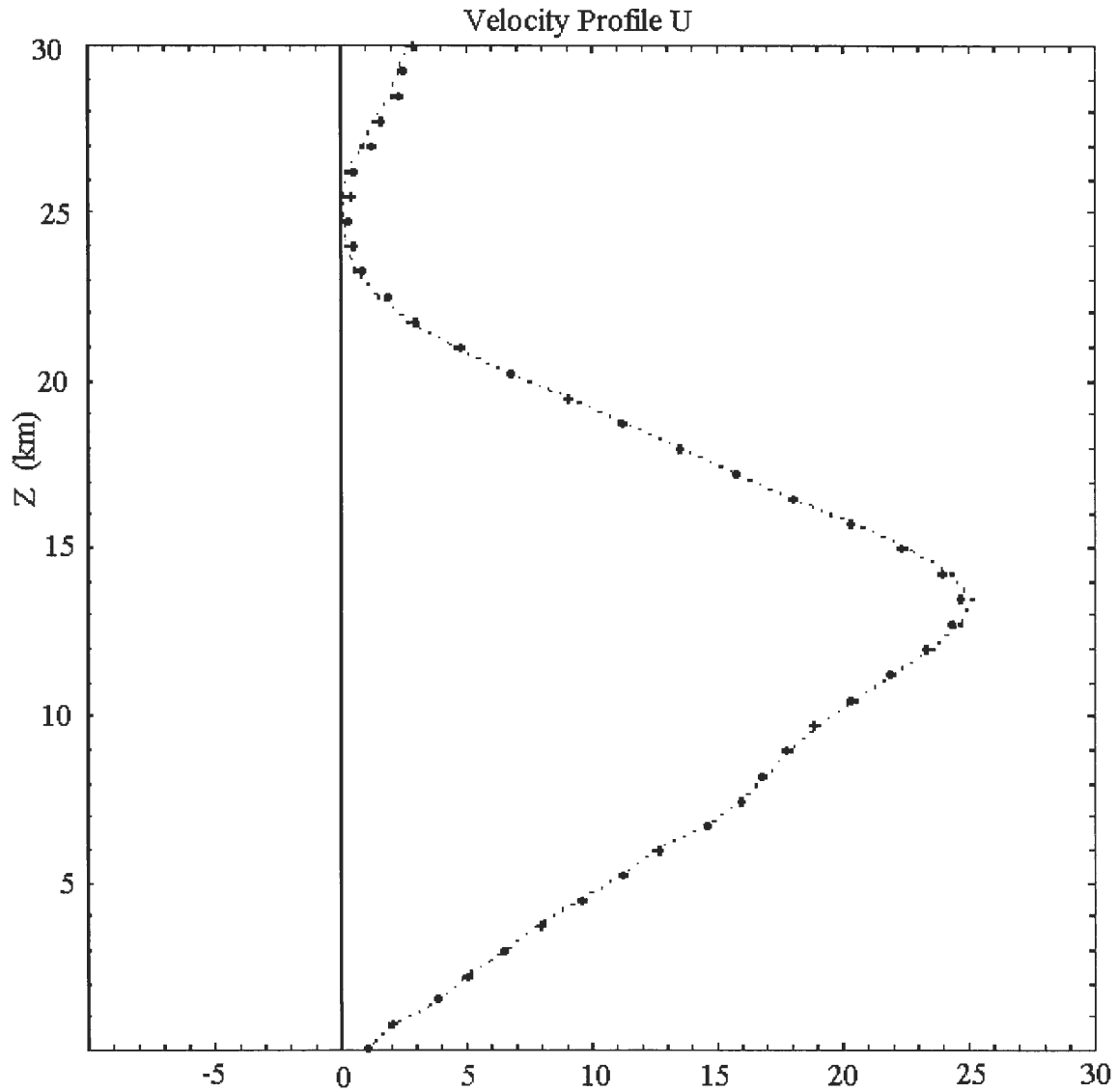


Fig. 14 The regionally and time averaged (30 longitude band over 48 hours) zonal wind profile used in the wave analysis. There are 3 profiles shown, corresponding to data at  $-35.73^\circ$  latitude (averaging in x only), data for a  $3.0^\circ$  latitude band centered about  $-35^\circ$  (averaging in x and y) and data for a  $6.0^\circ$  latitude band centered about  $-35^\circ$  (averaging in x and y).

#### 4.5 Locally Longitudinally Averaged Eddy Fluxes

Values for several different fields ( $u, v, w, \rho$ ) were extracted from the HR run with stretched grid and topography, and zonally averaged along a  $30^\circ$  longitude band centered on the mountain. From these the local vertical eddy flux of westerly momentum and the local meridional eddy flux of westerly momentum were computed, where eddies were departures from the longitudinal average over the  $30^\circ$  band. The eddy fields were computed for a 48-hour period starting from the targeted time of 297 days. Fig. 15 shows results for the eddy momentum for the period (38 – 48) hours.

The longitudinally averaged vertical eddy flux of westerly momentum was computed from

$$[(\rho u)^* v^*] = [(\rho u)v] - [\rho u][v] \quad (4.13)$$

and eddy flux of vertical momentum was computed from

$$[(\rho u^* w^*)] = [(\rho u)w] - [\rho u][w] \quad (4.14)$$

##### 4.5.1 Local horizontal eddy flux of westerly momentum

There are four distinct centers of momentum fluxes in both hemispheres (not shown). The momentum flux in the Northern Hemisphere is broader and much weaker than that in the Southern Hemisphere. In the Northern Hemisphere the center of the upward flux is centered to the north of  $30^\circ$ -latitude. Tropical areas of the Northern Hemisphere are influenced by the southward transport of westerly flux. However in the Southern Hemisphere we see a northward flux of horizontal momentum.

#### 4.5.2 Local vertical eddy flux of westerly momentum

Vertical eddy flux of westerly momentum is upwards (Fig 15) from the equator to about  $30^{\circ}$  S from the surface up to 4 km altitude. Above 4 km, the eddy flux of westerly momentum is downward. This occurs for a 10-hour period. During this time, two centers of momentum flux emerge, one below 2 km and the other around 5 km altitude. The area of maximum flux is in the tropics. A secondary maximum occurs at 4 km altitude just below the mountain. This appears to be consistent with our diagnosed gravity waves. The flux of westerly momentum intensifies briefly at  $t = 13$  hr. From  $t = 28$  hr, the upward flux of vertical momentum decreases and upward flux starts deepening at  $t = 30$  hours and grows with time in the midlatitudes. The westerly momentum is transported down from about 6 km to the surface between  $t = 39$  hr and 48 hr. As the downward flux of vertical momentum increases the upward flux of vertical momentum decreases from  $t = 28$  hr(not shown) onwards. The highest flux of momentum is in the Southern Hemisphere close to the source of what we diagnosed as gravity waves. The convergence and divergence in the momentum are large enough to change the zonal flow by several m/s over a 24-hr period. Figures from  $t = 38$ hr to  $t = 48$  hr are shown in Fig.15.

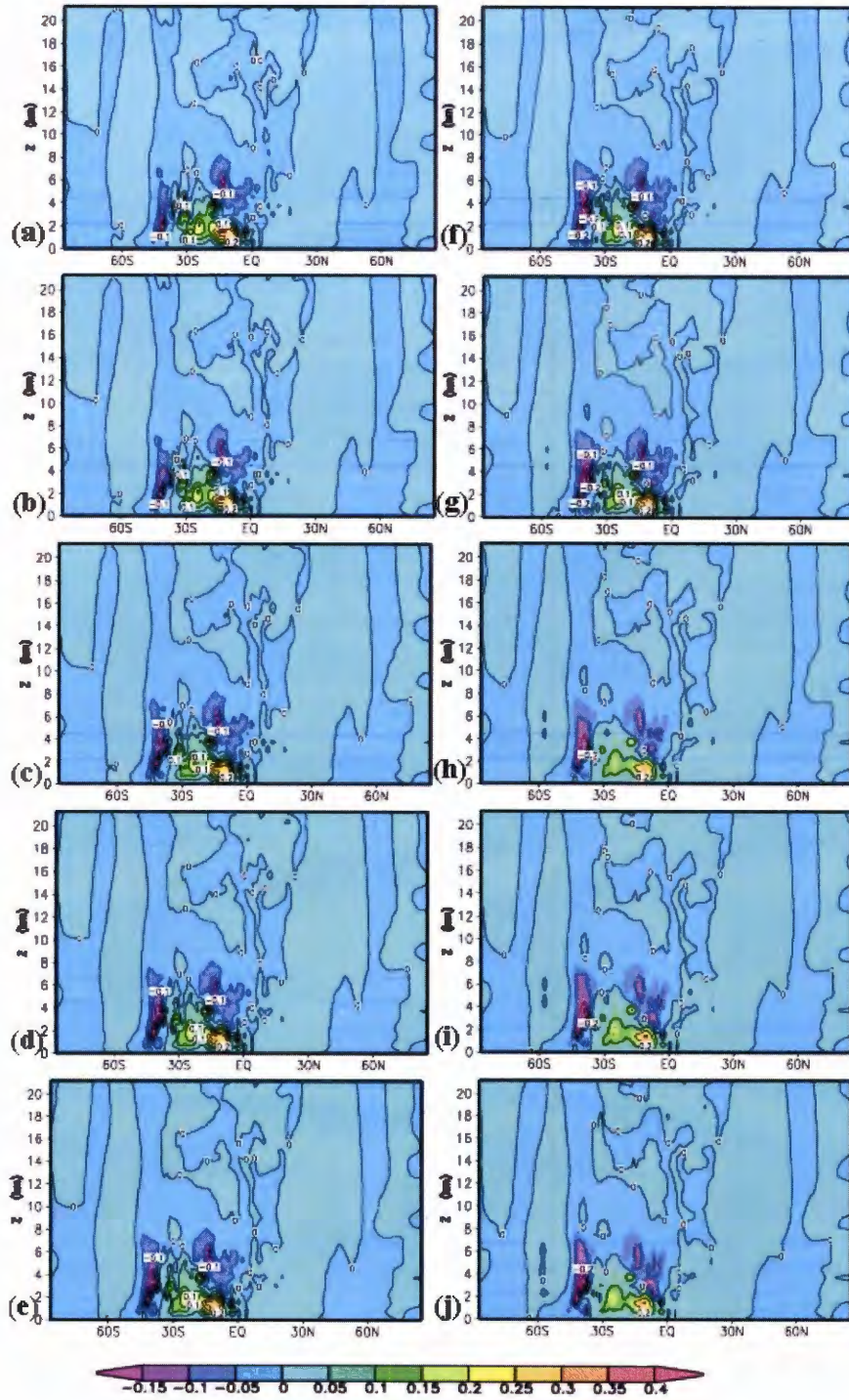


Fig.15 Simulations of longitudinally averaged vertical eddy flux of westerly momentum for the day 298 plus (a) 38 hr, (b) 39 hr, (c) 40 hr, (d) 41 hr, (e) 42 hr, (f) 43 hrs, (g) 44 hr, (h) 45 hr, (i) 46 hr, (j) 47 hr and (k) 48 hr from the targeted time of 297 days for HR with stretched grid.

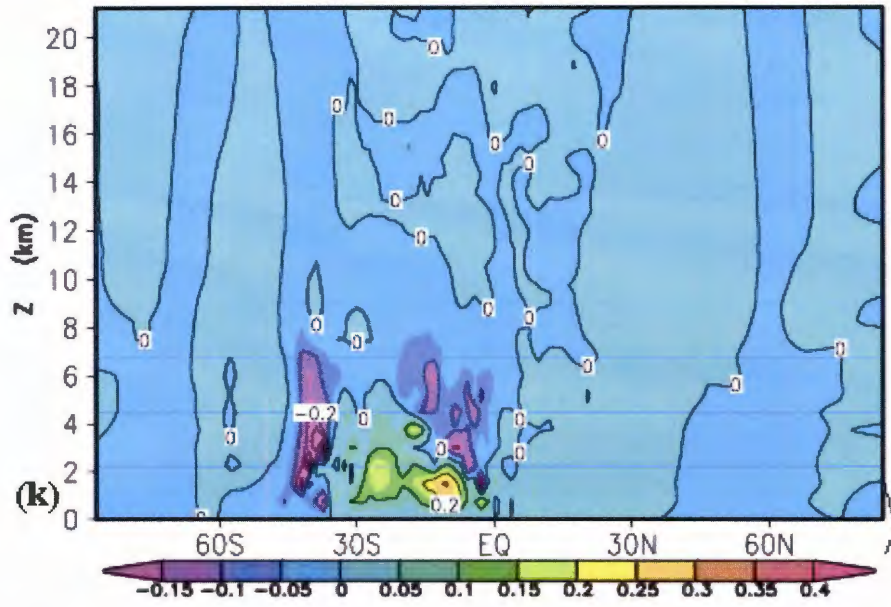


Fig. 15 (continued)

#### 4.6 Regional (two-dimensional) Simulations at Finer Resolution

Regional simulations of vertical wind were performed by Dr. J. Prusa using the same code that produced the global simulations, but configured to simulate a two dimensional (longitude–height) plane. The environment for these simulations was supplied by the full global runs, with the same type of mountain present in the middle of the domain. The more limited domain allowed higher resolution simulations whose output was analyzed for the presence of gravity waves. We used these simulations to examine effects of resolution on gravity-wave simulation that might be relevant to our three-dimensional simulations.

Regional simulations were done for  $-35^\circ$  latitude for several different resolutions, but we selected three resolutions, 300 km, 90 km and 40 km, for comparison with our HR runs. Fig 16 shows the vertical wind field and the vertical transport of westerly momentum for the 90-km case. The vertical wind (Fig. 16a) has a structure similar to the HR case. As the resolution gets finer (Fig. 17a), the  $w$  field's wave structure compares well with the 90-km



resolution case and the HR cases. However coarser resolutions (Fig.18) shows evanescent behavior in the wave and waves are more vertical.

The finer resolution (40-km) simulation shows behavior similar to the 90-km simulation, indicating that these resolutions are sufficient to simulate approximately the gravity waves in this environment. Also, the results in Fig. 16 and Fig. 17 for  $w$  were similar in appearance to our HRS GT results, so the 90-km and finer resolutions simulations would further support the result that the HRS GT simulation produced resolved gravity waves, but the LRS GT and HRUGT runs could not resolve them well. Also the regionally simulated lowest resolution run (Fig.18) was not able to resolve gravity waves well. The maximum vertical flux of westerly momentum for the 90-km resolution ( $0.125 \text{ kg m}^{-1}\text{s}^{-2}$ ) compares well with the maximum for the HR runs with a maximum of about  $0.2 \text{ kg m}^{-1}\text{s}^{-2}$  at  $35^\circ\text{S}$ . The vertical flux of westerly momentum from the HR run was sufficient to change the zonal flow by several m/s during one day.

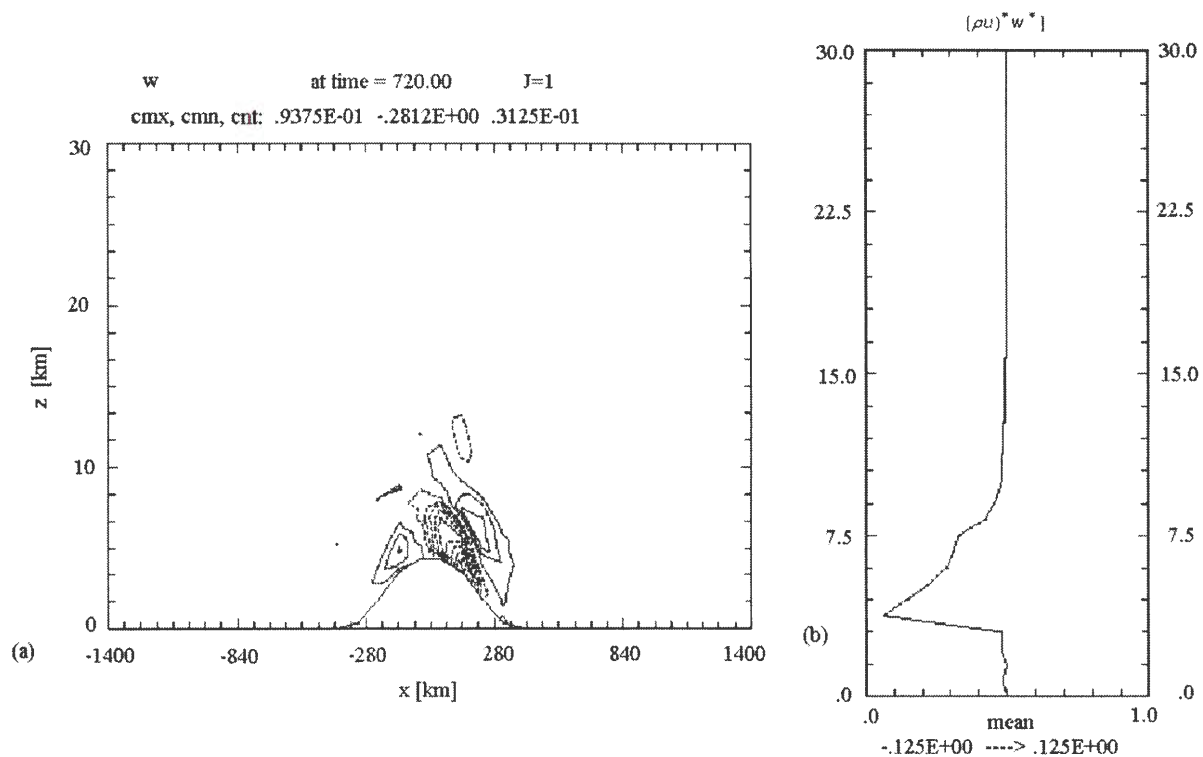


Fig. 16 Regional simulation of vertical wind and eddy flux of vertical momentum, using a grid spacing of 90 km. These simulations are for latitude 35° S. The horizontal scale is set by the peak half width, which is 280 km.

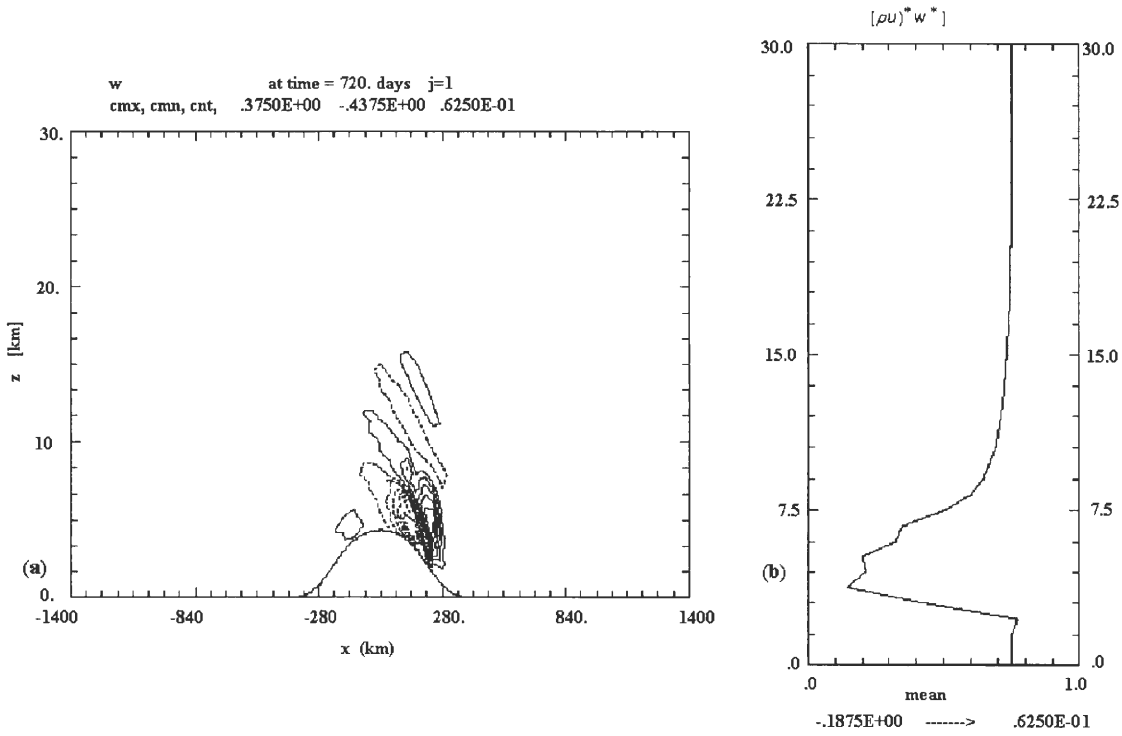


Fig. 17 Regional simulation of (a) vertical wind and (b) vertical flux of westerly momentum, using a grid spacing of 40 km. These simulations are for latitude -35° S. The horizontal scale is set by the peak half width, which is 280 km

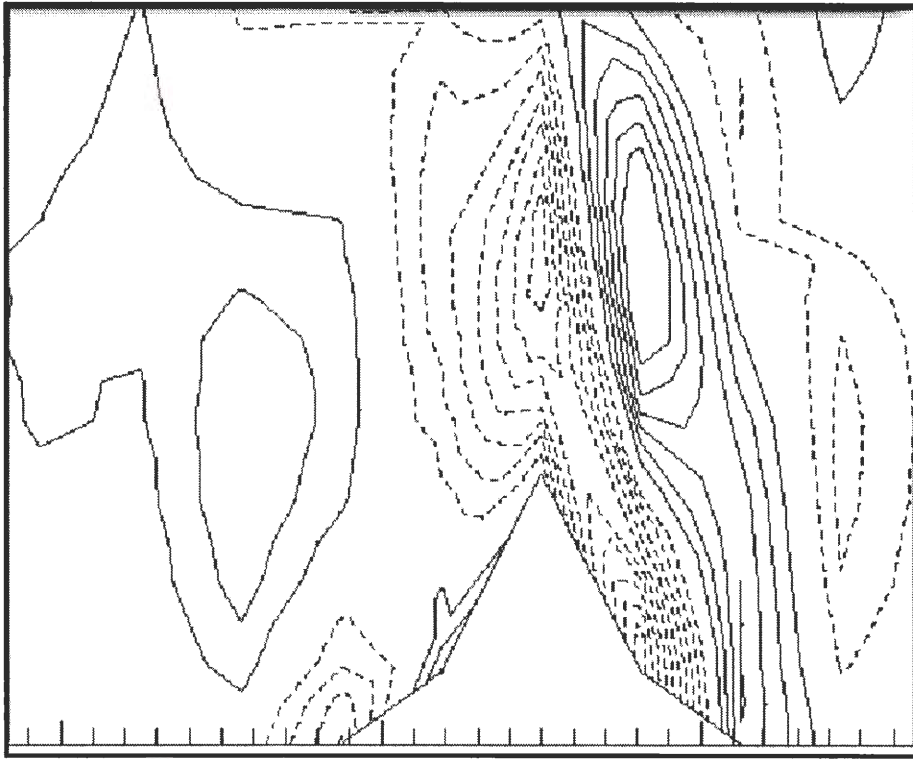


Fig. 18 Regional simulation of x-z cross-section of vertical wind, using a grid spacing of (a) 100 km and a time step of 4 min and (b) 300km and time step of 7.5 min. This simulation shows the evanescent behavior of waves. The waves are poorly resolved and vertical. These simulations are for latitude  $20^{\circ}$  S. The horizontal scale is set by the peak half width, which is 280 km.

## CHAPTER 5

### DISCUSSION AND CONCLUSIONS

#### 5.1 Summary

Global circulation was simulated with and without idealized topography at various resolutions. The different resolutions were used to search for the lowest resolution that would simulate gravity waves. Our control run with a symmetric forcing centered on the equator was sufficient to simulate general features of the large-scale atmosphere and therefore our model was adequate for our experiments. Zonal averages of zonal wind and westerly momentum fluxes were diagnosed for the different model simulations to examine the influence of resolution on these fields. We increased resolution either by stretching that concentrated the number of grid points over a portion of the Southern Hemisphere, at the expense of areas surrounding it, or by uniformly increasing the number of grid points over the whole globe. These had different effects on the jet maximum. For the low resolution (LR) case, increasing resolution through grid stretching yielded in the Southern Hemisphere a stronger zonal jet maximum, the jet maximum shifted polewards and upwards, and its latitudinal extent increased, though stretching had an opposite effect on the latitudinal shift in the Northern Hemisphere. For high-resolution (HR) cases, grid stretching resulted in a different behavior in the Southern Hemisphere compared to the LR cases, and the effect was the same as the LR cases in the Northern Hemisphere. When resolution was increased in the whole domain, maximum zonal wind decreased in the Southern Hemispheres. The decrease was largest for uniform grid (UG) cases (9 m/s) compared to the stretched (SG) cases (2 m/s).

Including a mountain in the model caused a decrease in the zonal wind in the Southern Hemisphere. The presence of topography in the model for low-resolution runs resulted in a decline in the maximum speed by 4 m/s in the Northern Hemisphere and no change in the latitudinal position of the jet in comparison to the LR-SG simulation with flat terrain (LRSGF). The jet maximum is lower in altitude than the flat terrain runs. The jet width for the LRSGT increased by about  $2^\circ$ . A similar behavior was observed for the UG runs. However, the jet maximum shifted polewards and maximum wind increased more, by 4 m/s.

When resolution was increased through grid stretching, the maximum flux increased in both hemispheres except for the stretched-grid HR case. Fluxes shifted poleward in the Southern Hemisphere and equatorward in the Northern Hemisphere for the topography cases, but they shifted equatorward in both hemispheres for the HR runs. The HR uniform and stretched grids resolved the meridional structures well as shown by the distinct extrema in the vertical eddy momentum flux field and consistent flux structure for the same fields, among different resolutions. However, the lowest resolution failed to resolve the meridional structures well compared to the higher resolution cases. The maximum wind coincided with centers of vertical eddy momentum flux convergence, indicating that these fluxes play a significant role in maintaining the large-scale zonal jets.

Gravity waves can develop when stable stratified air flows over a terrain; our model had an idealized mountain for the development of gravity waves. Since gravity waves transport momentum and change the zonal wind of their surroundings, we therefore extracted time series of the vertical flux of westerly momentum and of zonal wind to find periods to search for possible gravity waves. These were found by targeting periods when zonal wind

was changing rapidly and momentum flux was a maximum, because we assumed these behaviors might indicate episodes of strong wave-momentum convergence or divergence. When target periods had been identified, the model was re-run for these periods and the diagnostics saved every hour. From this data x-y cross-sections were made at 5.25 km altitude, close to the source of the waves, to search for wavelike behavior. This behavior was found to be more prominent in the HRSGT run. When the wavelike behavior had been established, we found the locations where it was more prevalent and filtered the data for that latitude to make x-z plots of the vertical motion field. The vertical motion field was allowed to pass through three types of filters in search of the one that would show clearly waves that had been well resolved. High-pass, low-pass and band pass-filters were used. The band-pass filter, which retained wave numbers 4-8 for a  $30^\circ$  longitude zone centered about the mountain, showed more wavelike behavior compared to other filters. Waves from LR and HR with uniform grid showed evanescent behavior in the vertical direction, and these waves were oriented almost vertically with height. Waves thus were well resolved at the highest resolution ( $1.4^\circ \times 0.9^\circ$ ) in the vicinity of the mountain, but not at lower resolutions.

Simulated zonally averaged vertical wind was used to measure wave properties such as wavelength (horizontal and vertical) and wave speed, which were then compared with waves from linear theory. Two cases were used to test this consistency. The first case assumed that the waves were stationary (which was approximately the behavior of the waves), and the horizontal wavenumber was assumed. The dispersion relationship gave a vertical wavelength comparable to the simulated value. In the second case the vertical and horizontal wavelengths were assumed and the phase speed obtained was 0.64 m/s, a value comparable to the simulated value of  $-0.5 \pm 1.0$  m/s. This value is consistent with our first

assumption that we made in the first case that our waves are stationary. Our simulated wave properties thus were consistent with the linear wave theory.

Simulated vertical flux of westerly momentum and the vertical wind fields were compared with 2-d regional, very high-resolution simulations (with grid spacing of 90 km, 40 km and 300 km). The simulated wave structure in the vertical wind field was similar in the 2-d results for waves at HR (90 km and 40 km) but the LR (300 km) results appeared evanescent in the vertical. This suggests:

- (a) That the HRS GT had sufficient resolution for gravity waves, and they matched well the behavior seen in the 2-d GW case.
- (b) That coarser resolution (300 km), which was roughly like our LRS GT and HRUGT resolutions near the mountain, gave evanescent structures that we can take to be an attempt by the model to produce gravity waves, but they are not well-resolved enough to appear.

The vertical flux of westerly momentum for the 2-d high resolution simulations ranged from  $(-0.125 \text{ to } 0.125) \text{ kg-m}^{-1}\text{-s}^{-2}$  for the 90 km simulation and  $(-0.19 \text{ to } 0.625) \text{ kg-m}^{-1}\text{-s}^{-2}$  for the 40-km simulation, which compared quite well in magnitude with a vertical flux of  $0.2 \text{ kg-m}^{-1}\text{-s}^{-2}$  near  $-35^\circ$  latitude for the HRS GT simulation. Furthermore, an estimated zonal wind acceleration using the 3-d simulation's vertical eddy fluxes in the lower atmosphere gave an acceleration of 8.6 m/s per day, a value similar to the daily fluctuations of velocity. This is evidence that the gravity waves were producing part of the 3-d simulation's acceleration and deceleration of the westerly flow near the mountain.



## 5.2 Conclusion

LR-resolution runs were not sufficiently fine to resolve properly gravity waves. The HR-resolution runs with stretched grid were able to resolve gravity waves well. Our 3-d simulations of vertical wind at HR were similar to the 2-d simulations at high resolutions; consequently we can say that our model resolved gravity waves. Resolutions of at least 90 km are needed to resolve properly gravity waves produced by our flow and mountain configuration.

Simulated vertical eddy fluxes were large enough to change the zonal flow because they generated zonal accelerations that were comparable to the daily fluctuations. The momentum flux thus can modify the large-scale flow.

## 5.3 Practical Applications

Our model was very simple with an idealized mountain and no moisture in it but our simulations were realistic as shown by the control run's zonal flow. This model can therefore be used to simulate the real world by adding real mountains and moisture to study the interactions of convective systems with the gravity waves in the Southern Hemisphere this is desirable since little such research has been done for this region. Increasing resolution to much finer levels in our current model can result in wave breaking. It would be interesting to see how this affects the momentum transfer to higher levels. Raising the level of the atmosphere will give us a more complete range of gravity-wave behavior.

## REFERENCES

- Clark, T. L., W. D. Hall, R. M. Kerr, D. Middleton, L. Radke, F. Ralph, and P. Neiman.,  
2000: Origins of aircraft-damaging clear-air turbulence during the 9 December 1992  
Colorado downslope windstorm: numerical simulations and comparison with  
observations. *J. Atmos. Sci.*, **57**, 1105–1131.
- de Villiers M.P., J. van Heerden , 2001: Clear air turbulence over South Africa  
*Meteorol. Appl.*, **8**, 119–126.
- Fox-Rabinovitz, M.S., G.L. Stenchikov, M.J. Suarez, L.L. Takacs, and R.C.  
Govindaraju, 2000: A uniform and variable resolution GCM dynamical core with  
realistic orography, *Mon. Wea. Rev.*, **128**, 1883-1898.
- Gal-Chen, T., and R.C.J. Somerville, 1975: On the use of a coordinate transformation for the  
solution of the Navier-Stokes equations. *J. Comput. Phys.*, **17**, 209-228.
- Garcia, R.R., and S. Solomon, 1985: The effect of breaking gravity waves on the dynamics  
and chemical composition of the mesosphere and lower thermosphere. *Geophys. Res.*,  
**90**, 3850-3868.
- Holton J.R., 1982: The role of gravity wave induced drag and diffusion in the momentum  
budget of the mesosphere. *J. Atmos. Sci.*, **39**, 791-799.
- Holton J.R., 1983: The influence of gravity wave breaking on the general circulation of the  
middle atmosphere. *J. Atmos. Sci.*, **40**, 2497-2507.
- Holton J.R., 1992: An Introduction to Dynamical Meteorology (Third Ed.). Academic Press,  
San Diego California, 511pp.
- Hooke W. H., 1986: Gravity Waves in Mesoscale Meteorology and Forecasting. American  
Meteorological Society, Boston, MA edited by P.S. Ray, 793pp.

- Held, I.M. and M.J. Suarez 1994: A proposal for the intercomparison of the dynamical cores of atmospheric general circulation model. *Bull. Amer. Meteor. Soc.*, **75**, 1825-1830.
- Keller, T.L., 1993: Implications of the hydrostatic assumption on atmospheric gravity waves. *J. Atmos. Sci.*, **51**, 1915-1929.
- Kim, Y-J., 1996: Representation of sub-grid scale orographic effects in a general circulation model. Part I: Impacts on the dynamics of simulated January climate. *Bull. Amer. Meteor. Soc.*, **9**, 2698-2717.
- Knox, J.A., 1997: Possible mechanisms of clear-air turbulence in strongly anticyclonic flows. *Mon. Wea. Rev.*, **125**, 1251-1259.
- Lilly, D.K., and P.J. Kennedy, 1972: Wave momentum flux: A GARP problem. *Bull. Amer. Meteor. Soc.*, **53**, 17-23.
- Lilly, D.K., and P.J. Kennedy, 1973: Observations of a stationary mountain wave and its associated momentum flux and energy dissipation. *J. Atmos. Sci.*, **30**, 1135-1152.
- Lindzen, R.S., 1981: Turbulence and stress owing to gravity wave and tidal breakdown. *J. Geophys. Res.*, **86**, 9707-9714.
- Lipps, F.B., and R.S. Hemler, 1982: A scale analysis of deep moist convection and some related numerical calculations. *J. Atmos. Sci.*, **39**, 2192-2210.
- McFarlane N.A., 1987: The effect of orographically excited gravity wave drag on the general circulation of the lower stratosphere and troposphere. *J. Atmos. Sci.*, **44**, 1775-1800.
- Palmer, T.N., G.J. Shutts, and R. Swinbank, 1986: Alleviation of a systematic westerly bias in general circulation and numerical weather prediction models through an orographic-gravity wave drag parameterization. *Quart. J. R. Met. Soc.*, **112**, 1001-1039.

- Peixoto, J.P., A.H.Oort, 1992: Physics of Climate. American Institute of Physics, New York, 520pp.
- Prusa, J.M., P.Smolarkiewicz, and R.R Garcia, 1996: Propagation and breaking at high altitudes of gravity waves excited by tropospheric forcing. *Ame. Meteor. Soc.*, **53**, 2186-2216.
- Prusa, J.M., P.Smolarkiewicz, 2003: An all-scale anelastic model for geophysical flows: dynamic grid deformation. *J. Comput. Phys.* **190**, 601-622.
- Slingo, A., and D.W. Pearson, 1987: A comparison of the impact of an envelope orography and of a parameterization of orographic gravity-wave drag on model simulations. *Quart. J. Roy. Meteorol. Soc.*, **113**, 847-870.

## ACKNOWLEDGEMENT

I am mostly grateful to my advisor Dr William Gutowski for imparting his knowledge, explaining many concepts and his great patience that enabled me to complete this research. My sincere gratitude goes to Dr J. Prusa the author of the code we used. Without it this work would not have been accomplished and his tireless efforts in explaining the code and various concepts. Thanks to Dr. Joseph Prusa and Dr. William Gutowski and Dr. Babatunde Abiodun for supplying some of the figures and doing some of the calculations. My gratitude goes to Daryl Herzmann for his dedicated computing support throughout this project. Francis Otieno and Eric Aligo were very helpful in explaining some concepts and teaching me how to use some software, without their help I would never have completed this research. I am very grateful to the Department of Energy for their grant and their continued support for this work for these past 2 and half years and the faculty in the Meteorology Department at Iowa State University for their wealthy of knowledge. Last but not least I am indebted to the government of Zimbabwe for granting me leave so I could come and study and my mum and Meteorology Club at Iowa State University and close friends for their moral support.